Time-delay Measurement of Mg II Broad-line Response for the Highly Accreting Quasar HE 0413-4031: Implications for the Mg II–based Radius–Luminosity Relation

Michal Zajaček[1] , Bożena Czerny[1] , Mary Loli Martinez–Aldama[1] , Mateusz Rałowski[1] , Aleksandra Olejak[1] ,
Swayamtrupta Panda[1,2] , Krzysztof Hryniewicz[2] , Marzena Śniegowska[1] , Mohammad-Hassan Naddaf[1] , Wojtek Pych[2],
Grzegorz Pietrzyński[2] , C. Sobrino Figaredo[3] , Martin Haas[3] , Justyna Średzińska[2], Magdalena Krupa[4], Agnieszka Kurcz[4],
Andrzej Udalski[5] , Marek Gorski[6] , and Marek Sarna[2]

[1] Center for Theoretical Physics, Polish Academy of Sciences, Al. Lotników 32/46, 02-668 Warsaw, Poland; zajacek@cft.edu.pl
[2] Nicolaus Copernicus Astronomical Center, Polish Academy of Sciences, ul. Bartycka 18, 00-716 Warsaw, Poland
[3] Astronomisches Institut—Ruhr Universitaet Bochum, Germany
[4] Astronomical Observatory of the Jagiellonian University, Orla 171, 30-244 Cracow, Poland
[5] Astronomical Observatory, University of Warsaw, Al. Ujazdowskie 4, 00-478 Warsaw, Poland
[6] Departamento de Astronomia, Universidad de Concepcion, Casilla 160-C, Chile
Received 2019 October 29; revised 2020 May 17; accepted 2020 May 17; published 2020 June 23

Abstract

We present the monitoring of the active galactic nuclei continuum and Mg II broad-line emission for the quasar HE 0413-4031 ($z = 1.38$) based on the six-year monitoring by the South African Large Telescope (SALT). We manage to estimate a time-delay of $302.6^{+28.7}_{-33.1}$ days in the rest frame of the source using seven different methods: interpolated cross-correlation function, discrete correlation function (DCF), z-transformed D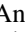CF, JAVELIN, two estimators of data regularity (Von Neumann, Bartels), and χ^2 method. This time-delay is below the value expected from the standard radius–luminosity relation. However, based on the monochromatic luminosity of the source and the spectral energy distribution modeling, we interpret this departure as the shortening of the time-delay due to the higher accretion rate of the source, with the inferred Eddington ratio of ∼0.4. The Mg II line luminosity of HE 0413-4031 responds to the continuum variability as $L_{\rm line} \propto L_{\rm cont}^{0.43\pm0.10}$, which is consistent with the light-travel distance of the location of Mg II emission at $R_{\rm out} \sim 10^{18}$ cm. Using the data of 10 other quasars, we confirm the radius–luminosity relation for the broad Mg II line, which was previously determined for the broad Hβ line for lower-redshift sources. In addition, we detect a general departure of higher-accreting quasars from this relation in analogy to the Hβ sample. After the accretion-rate correction of the light-travel distance, the Mg II–based radius–luminosity relation has a small scatter of only 0.10 dex.

Unified Astronomy Thesaurus concepts: Accretion (14); Active galaxies (17); Quasars (1319); Radio-loud quasars (1349); Supermassive black holes (1663); Quasars (1319); Spectroscopy (1558)

1. Introduction

Reverberation mapping (RM) of active galactic nuclei (AGNs) is a leading method to study the spatial scale as well as the structure of the broad-line region (hereafter BLR; see Blandford & McKee 1982; Peterson & Horne 2004; Gaskell 2009; Czerny 2019). The method is very time consuming because it requires tens or even hundreds of spectra, covering well the characteristic timescales in a given object. Collected data allow for the measurement of the time-delay of a chosen emission line with respect to the continuum. Assuming light-travel time of light propagation, we thus obtain the characteristic size of the BLR. Subsequent discovery of the relation between the size of the BLR and the source of absolute monochromatic luminosity (Kaspi et al. 2000; Peterson et al. 2004; Bentz et al. 2013) opened a way to measure black hole masses in large quasar samples using just a single-epoch spectrum (e.g., Collin et al. 2006; Vestergaard & Peterson 2006; Shen et al. 2011; Mejía-Restrepo et al. 2018).

The radius–luminosity relation based on the monitoring of the broad Hβ component is relatively well studied in the case of lower-redshift sources, including nearby quasars (below ∼0.9; Kaspi et al. 2000; Bentz et al. 2013; Grier et al. 2017). For larger redshifts, Hβ moves to the infrared bands, and in the optical band, the spectrum is dominated by UV emission lines. Sources with redshifts in the range of ∼0.4–1.5, when the

spectrum is observed in the optical band, become dominated by the Mg II line, and at higher redshifts C IV moves into the optical band. Thus, the single-spectrum methods are used to scale the Hβ and the other line properties (mostly systematic differences in the line widths) to be able to cover a large spectral range. Direct reverberation measurements in other lines than Hβ are still rare. In the current paper, we show a new reverberation measurement done in the Mg II line for the redshift larger than one.

The Mg II line seems to be suitable for the black hole mass measurements because, together with Hβ, it belongs to the low-ionization lines (Collin-Souffrin et al. 1988), and thus should originate close to the accretion disk, where the motion of the emitting material is largely influenced by the potential of the central black hole. Therefore the motion of the Mg II-emitting material is expected to be quasi-Keplerian, i.e., the velocity field is dominantly Keplerian with a certain turbulent component. In analogy to the Hβ broad component, the Mg II line is virialized (Marziani et al. 2013), while high-ionization lines exhibit clear line profile asymmetries that imply the outflowing motion and the importance of the radiation force.

On the other hand, monitoring of Mg II is more difficult because the line in many sources has very low variability amplitude (Goad et al. 1999; Woo 2008; Zhu et al. 2017; Guo et al. 2020) and/or the timescales at larger redshifts and for more massive (and luminous) quasars are considerably longer.

Also the width of the Mg II line is narrower than the Hβ broad component, which indicates the position at larger light-travel distances (Marziani et al. 2013). In addition, the Mg II line-emitting gas is evidenced to respond to nonthermal radiation from jets, which may further complicate the RM for radio-loud and γ-ray emitting sources (León-Tavares et al. 2013; Chavushyan et al. 2020).

Successful determination of the line time-delay has been achieved only for 10 sources so far (Metzroth et al. 2006; Shen et al. 2016; Grier et al. 2017; Lira et al. 2018; Czerny et al. 2019), but it nevertheless allowed for the preliminary construction of the radius–luminosity relation based on the Mg II line (Czerny et al. 2019) with the slope close to $R \propto L^{0.5}$ (Panda et al. 2019b) being consistent with the relation for the Hβ line (Bentz et al. 2013). The key measurement toward larger luminosities came from the bright quasar CTS C30.10 ($z = 0.90052$, $\log [L_{3000}(\mathrm{erg\,s^{-1}})] = 46.023$) monitored for 6 yr with the South African Large Telescope (SALT). The source CT252, for which the RM was also performed in Mg II line (Lira et al. 2018), alongside CIII] and C IV monitoring, so far had the largest redshift of $z = 1.890$ among Mg II sources.

In this paper, we show the results for the quasar HE 0413-4031 also monitored with the SALT, but brighter ($\log [L_{3000}(\mathrm{erg\,s^{-1}})] = 46.741$) and located at the redshift of $z = 1.389$ (according to NED[7]). This quasar was found as part of the Hamburg/ESO survey for bright QSOs (Wisotzki et al. 2000). Apart from the quasar spectrum, the source is also radio-loud and belongs to the flat-spectrum radio quasars (FSRQ)—blazars (Mao et al. 2016). In fact, according to the NED database, the radio spectral slope at lower radio frequencies between 0.843 GHz and 5 GHz is inverted with $\alpha = 0.68$,[8] which indicates a compact self-absorbed radio core. From this, we estimate the flux density at 1.4 GHz, $F_{1.4} \approx 21$ mJy, which implies the monochromatic luminosity per frequency of $L_{1.4} \approx 2.5 \times 10^{26}\,\mathrm{W\,Hz^{-1}} > 10^{24}\,\mathrm{W\,Hz^{-1}}$, based on which HE 0413-4031 can be classified as radio-loud AGN (Tadhunter 2016).

In the analysis, we determine the rest-frame time-delay of the Mg II line using different statistically robust methods—interpolated cross-correlation function (ICCF), discrete correlation function (DCF), z-transformed DCF, JAVELIN, two estimators of data regularity (Von Neumann, Bartels), and χ^2 method. The determined rest-frame time-delay of ∼303 days turns out to be smaller than the time-delay predicted from the expected radius–luminosity relation, where the radius of the BLR is proportional to the square root of the monochromatic luminosity. Because HE 0413-4031 is a quasar with the accretion rate close to the Eddington limit, which is inferred from the detailed spectral energy distribution (SED) fitting, we demonstrate that the shortening of the measured time-delay is due to the accretion-rate effect in analogy to the Hβ-based radius–luminosity relation (Martínez-Aldama et al. 2019).

The paper is structured as follows. In Section 2, we present the observational analysis including both spectroscopy and photometry. Subsequently, in Section 3, we analyze the mean spectrum, rms spectrum, spectral fits of individual observations, and the variability properties of lightcurves. The focus of the paper is on the time-delay determination of the Mg II broad-line emission with respect to the continuum using different statistical methods, which is presented in detail in Section 4. In

Section 5, we present the preliminary virial black hole mass and Eddington ratio, and using other measurements of Mg II time-delay, we construct a Mg II–based radius–luminosity relation and demonstrate that the departure of the sources depends on their accretion rate, which leads to the significant time-delay shortening for the highly accreting quasar HE 0413-4031. In the discussion part in Section 6, we discuss the nature of Mg II emission in terms of the source classification along the quasar main sequence, taking into account its radio properties. In addition, we analyze the response of the Mg II line with respect to the continuum variability, which is related to the intrinsic Baldwin effect, and we perform the SED fitting to obtain independently the black hole mass and other parameters related to accretion. Finally, we summarize the main conclusions in Section 7.

2. Observations

The quasar HE 0413-4031, located at redshift $z = 1.389$ according to the NED database, is a very bright source: Véron-Cetty & Véron (2001) report the V magnitude of $M_V = 16.5$ mag. Its position on the sky ($04^\mathrm{h}\ 15^\mathrm{m}\ 14^\mathrm{s}$; $-40°\ 23'\ 41''$) made it a very good target for the spectroscopic monitoring with the SALT. The source was monitored from 2013 January 21 until 2019 August 8. The spectroscopic and photometric data are summarized in Section A in Tables A1–A3.

2.1. Spectroscopy

The quasar was observed using the Robert Stobie Spectrograph on SALT (RSS; Burgh et al. 2003; Kobulnicky et al. 2003; Smith et al. 2006). A slit spectroscopy mode was used, with the slit width of 2″. Adopted medium resolution grating PG1300 and the grating angle of 28.625, with the filter PC04600, gave a configuration of a spectral resolution of 1523 at 7370 Å. The same configuration has been used in all 25 observations, covering more than six years. A single exposure usually lasted about 820 s, and two exposures were taken during each observation. All observations were performed in service mode. The observation dates are given in Table A1.

The basic reduction of the raw data was done by the SALT staff by applying a semiautomatic pipeline that was a part of the SALT PyRAF package. At the next stage the two images were combined with the aim to remove the cosmic rays as well as to increase the signal-to-noise ratio. The wavelength calibration was performed using the calibration lamp exposures taken after the source observation. In most observations argon lamp was used. Additionally, we checked the calibration using the OI sky line 6863.955 Å because in our observations of another quasar with SALT, the lamp calibration was not very accurate at early years of monitoring. However, for HE 0413-4031 the differences between the lamp calibration and the sky line position were at a level of a fraction of an Angstroem.

Due to the specific design of the SALT, correcting for vignetting is an important issue. For that purpose we used an ESO standard star LTT 4364 (white dwarf, with practically no spectral features in the interesting spectral range), which was observed with SALT in the same configuration as the quasar. Through analytic parameterization of the ratio of ESO and SALT spectrum of the star, we obtained a correction to the spectral shape of a quasar in the observed wavelength range from 6342 to 6969 Å in the observed frame. Formally, the part

---

of the spectrum up to 8600 Å is available, apart from two gaps, but the correction of the spectral shape by the comparison star is not satisfactory in this spectral range. Absolute calibration of the SALT spectra was performed using the supplementary photometry.

2.2. Photometry

Spectroscopic observations were accompanied by denser photometric monitoring. For a significant part of our campaign, high-quality data were collected as part of the OGLE-IV survey done with the 1.3 m Warsaw telescope at the Las Campanas Observatory, Chile. Monitoring was performed in the V band, with the exposure time 240 s, and the typical error was about 0.005 mag.

We also obtained photometric measurements from the SALT on the same night as the spectroscopic observations were performed, whenever the instrument SALTICAM was available. We used the images obtained in g band; usually two exposures were made, with the exposure time 45 s. Because the SALT instrument is not suitable for highly accurate photometric observations, the typical error of this photometry is of the order of 0.012 mag. Because SALTICAM data were collected in a different band from OGLE, we allowed for a grayshift of the SALTICAM set using the periods when the two monitorings overlapped.

Finally, in the period between 2017 December 3 and 2019 March 24, we also performed short, denser monitoring with the 40 cm Bochum Monitoring Telescope (BMT), based at the Universitaetssternwarte Bochum, near Cerro Armazones in Chile.[9] This monitoring was done in two bands, B and V, but for the purpose of this work only V-band lightcurve has been used. This data set is not entirely consistent with the OGLE + SALTICAM data; there appears to be a slight offset by 0.171 mag, when comparing the earliest BMT point with the last OGLE point. We corrected the magnitude of all the BMT points by this offset, i.e., increasing their magnitudes by 0.171 mag to match the first BMT point with the nearest OGLE point. For comparison, we performed time-delay measurements with this data subset included or not included in the photometric lightcurve. The photometric data points are listed in Tables A2 and A3.

2.3. Spectroscopic Data Fitting

We use the same approach to the modeling of the Mg II region as in Czerny et al. (2019). Because of the potential problems with the remaining vignetting effect, we concentrate only on the relatively narrow spectral band, from 2700 to 2900 Å, in the quasar rest frame. We allow for the following components: (i) power-law component of arbitrary slope and normalization, representing the continuum emission from the accretion disk; (ii) Fe II pseudo-continuum modeled using theoretical templates of Bruhweiler & Verner (2008), folded with a Gaussian of the width representing the kinematic velocity of the Fe II emitter; and (iii) the Mg II line itself. We also test other Fe II templates for completeness, but we discuss this issue separately, in Appendix C.

In our model, the Mg II line is parametrized in general by two separate kinematic components, each modeled assuming a Gaussian or a Lorentzian shape. The amplitudes, the width, and

the separation are the model parameters. Each kinematic component in turn is modeled as a doublet, and the ratio within the doublet components (varying from 1 to 2) depends on the optical depth of the emitting cloud.

The additional parameter is the source redshift, because the determination of the redshift in the NED database is not accurate enough for our data. Because we do not have an independent measure of the redshift from narrow emission lines, we assume that Fe II and one of the Mg II components represent the source rest frame.

All model parameters are fitted together; we do not first fit the continuum, because in the presence of the Fe II pseudo-continuum there is no clear continuum-dominated region and fitting all components at the same time is more appropriate. However, we differentiate between the global parameters and the parameters when modeling individual spectra. We first created a composite spectrum by averaging all observations; for such an average spectrum we determined the redshift, the best Fe II template and the Fe II smearing velocity, and the best value of the doublet ratio, and these values were later kept fixed when individual data sets were modeled.

We calculate the equivalent width (EW) of the lines with respect to the power-law component, within the limits where the model was applied (i.e., integrating between 2700 and 2900 Å). Calculation is done from the model, by numerical integration, and EW(Mg II) contains both kinematic and doublet components.

The reported errors of the fit parameters, including the errors of EWs of Mg II and Fe II, were determined by construction of the error contours—that is, computations for an adopted range of the parameter of interest, with all other parameters allowed to vary. This leads in general to asymmetric errors around the best-fit value. For the requested accuracy, we adopted the χ^2 increase by 2.706, appropriate for one parameter of interest, which represents a 90% confidence level (statistical significance 0.1).[10]

2.4. Spectroscopic Flux Calibration and Mg II Absolute Luminosity

The approach to data fitting outlined in Section 2.3 allows only for deriving EW of the Mg II and Fe II lines. However, computations of time-delay require the knowledge of the continuum lightcurve and the line luminosity lightcurve.

A continuum lightcurve is provided by the photometric monitoring, and we use this photometry to calibrate the SALT spectra and to determine the Mg II line flux.

Because we have three instruments providing us with the photometry, and they are of a different quality, as explained in Section 2.2, we first perform the interpolation of the photometry data points at the epochs for which the EW of Mg II is available using the weighted least-squares linear B-spline interpolation, using the inverse of photometry uncertainties as the corresponding weights in the spline interpolation algorithm.

Having established the photometric flux at the time of the spectroscopic measurements still does not allow us to obtain the calibrated spectrum easily. The V band does not overlap with the wavelength covered by our spectroscopy (see Section 2.1), and the redshift of our source ($z = 1.389$) corresponds to the rest-frame wavelength of 2304 Å. Therefore,

---

we have to interpolate between the *V* band and the median of our fitting band, 2800 Å rest frame. Because the measurement of the continuum slope in our narrow wavelength range is not very precise, and the slope changes between observations, the use of this slope could introduce an unnecessary scatter into the line flux calibration. Therefore we decided to use the broadband quasar continuum spectrum of Zheng et al. (1997) [11] as a template, and we assumed that the ratio between the flux at 2304 Å (corresponding to the *V* band in our quasar) and a continuum at 2800 Å in HE 0413-4031 is always the same as in the template.

This gave us a relation between the *V* magnitude and the 2800 Å continuum νF_ν flux at 2800 Å, F_{2800}:

$$\log F_{2800} = -0.4V - 8.234 \ [\text{erg s}^{-1} \text{cm}^{-2}] \qquad (1)$$

This is of course an approximation, but the amplitude of the flux variations in our source is not very large so the issue of a spectrum becoming bluer when the quasar is brighter (see, e.g., Ulrich et al. 1997; Wilhite et al. 2005; Kokubo 2015, and the references therein) should not be critical.

3. Results: Spectroscopy

3.1. Mean Spectrum

We first combined the SALT spectra in order to establish the global source parameters, which will be fixed later in the analysis of all 25 spectra.

The mean spectrum is shown in Figure 1 (top panel). For comparison, in Figure 1 (middle panel) we also show the spectrum in the early epoch (#5), when the quasar was close to the minimum flux density, as well as the spectrum from the later epoch close to the maximum flux density (#20, bottom panel). The Mg II line shape in this quasar looks simple, immediately suggesting that HE 0413-4031 belongs to class A quasars (Sulentic et al. 2000). We checked that assuming just a single kinematic component of Lorentzian shape for Mg II is sufficient, and adding the second component does not improve the χ^2 significantly. The best fit for a 2-component model allows for 0.2% contribution from the second kinematic component, which is very broad (11,140 km s^{-1}), and the total χ^2 for such a fit is better than in a single-component fit only by 1.0. The source is thus a typical representative of class A sources. We also checked that a Lorentzian shape offers much better representation of the line shape than the Gaussian. If we assume a single kinematic component with a Gaussian shape, the reduced χ^2 of the best fit is 16.0 per degree of freedom. If we allow for 2 Gaussian kinematic components, one with no shift with respect to Fe II and the second one at arbitrary position, the fit improves (reduced $\chi^2 = 7.7$) but still does not match the one with a single Lorentzian shape, despite the higher number of parameters. We note that in the case of the 2-Gaussian fit, the component bound to Fe II dominates (contains 57% of the line flux), which happened at the expense of the overall Fe II contribution, which dropped down by a factor of 3 in comparison with a single Lorentzian fit. However, such a fit is not favored by the data. The single-component Lorentzian profile typical of population A sources (Sulentic et al. 2000) arises due to the turbulence in the line-emitting clouds, and the broadening of the line is due to the rotation (Kollatschny & Zetzl 2011; Goad et al. 2012; Kollatschny & Zetzl 2013a, 2013b).
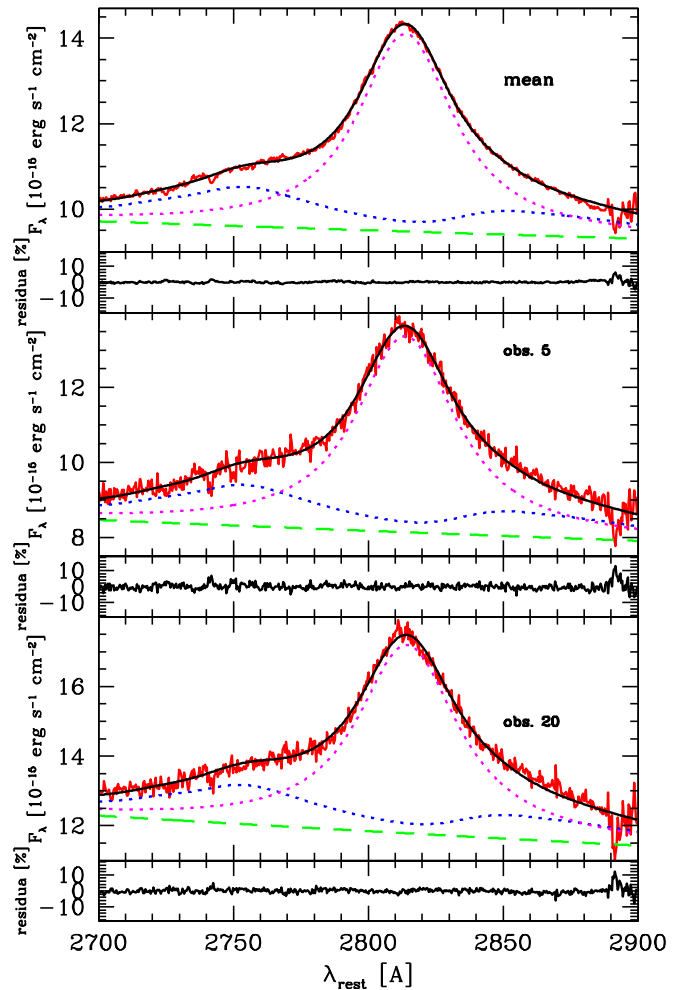
―――――――――――――――――
[11] Downloaded from https://archive.stsci.edu/prepds/composite_quasar/.

Figure 1. Top: flux-calibrated mean spectrum of HE 0413-4031. Data are shown with a red line, and the black line gives the best-fit model. Remaining lines show the spectral components: power law (green dashed line), Fe II pseudo-continuum (blue dotted line), and Mg II total flux (two doublet components, magenta dotted line). The lower panel shows the residua, which are noticeable only close to 2900 Å, where the sky line contamination was the strongest and the background subtraction did not fully correct for this effect. Middle: flux-calibrated spectrum of HE 0413-4031 for the minimum phase (epoch 5). The lines represent the same spectral components as in the top panel. Bottom: flux-calibrated spectrum of HE 0413-4031 for the maximum phase (epoch 20). The lines represent the same spectral components as in the top panel. The epochs are listed in Table A1.

Because in our full model one of the kinetic components was set at zero rest-frame velocity, together with Fe II, while the second kinematic component has an arbitrary shift in velocity space with respect to them, we eliminated the first kinematic component, leaving the second one, which allows for the flexibility of the shift between Mg II and Fe II. This model is also later used to fit individual spectra.

We tested several templates of the Fe II from Bruhweiler & Verner (2008), and the best fit was provided by the d12-m20-20-5.dat model, which assumes the cloud number density 10^{12} cm^{-3}, the turbulent velocity 20 km s^{-1}, and the hydrogen ionizing photon flux $10^{-20.5}$ cm^{-2} s^{-1}. The same template was favored for the quasar CTS C30.10 also monitored by SALT (Czerny et al. 2019). It is not surprising, because recent modeling of the quasar main sequence also suggest values of that order for the local BLR cloud density and the turbulent

velocity (Panda et al. 2018, 2019a). The best-fit half-width of the Gaussian used for template convolution was 1200 km s^{-1}.

We calculated a grid of models for different redshift and different ratio of the doublet, and these two quantities are strongly coupled. We determined the best-fit redshift as $z = 1.37648$, and the doublet ratio as 1.9. This is a value quite close to the optically thin case, 2:1 ratio.

These parameters—the choice of the Fe II template, template smearing velocity, redshift, and doublet ratio—were later assumed to be the same in all fits of the individual spectra, while the Fe II amplitude, Mg II amplitude, line width and line shift, and power-law parameters were allowed to vary from observation to observation.

The best-fit FWHM of the Mg II line in the mean spectrum is 4380^{+14}_{-15} km s^{-1}, formally just above the line dividing the class A and class B source (Sulentic et al. 2000; Marziani et al. 2018). However, some trend with the mass in this division is expected, because for Seyfert galaxies the dividing line between Narrow Line Seyfert 1 galaxies and Seyfert galaxies is at 2000 km s^{-1} (Osterbrock & Pogge 1985), instead of at 4000 km s^{-1}, as in quasars. HE 0413-4031 is still more massive and brighter than most quasars in Sloan Digital Sky Survey (SDSS) catalogs (Shen et al. 2011; Pâris et al. 2017). Because we fit the single Lorentzian shape, we cannot derive the line dispersion σ from the fit, because the Lorentzian shape corresponds to the limit of FWHM/$\sigma \to 0$. We can, however, determine the line dispersion numerically because the FWHM/σ ratio is an important parameter (Collin et al. 2006). Therefore, we subtracted the fitted Fe II and the remaining underlying continuum, and integrated the line profile. We obtained $\sigma = 2849$ km s^{-1}, and FWHM/$\sigma = 1.54$, which confirms that the source belongs to Population 2 of Collin et al. (2006), or class A of Sulentic et al. (2000).

In the mean spectrum, the EW(Mg II) is $27.45^{+0.12}_{-0.10}$ Å, a bit below the average value for the Mg II from Large Bright Quasar Sample (42 Å, Forster et al. 2001).

The most interesting part is the shift we detect between the Mg II line and the Fe II pseudo-continuum. This shift is by 15.1 Å, or equivalently, 1620 km s^{-1}, and the Mg II line is redshifted with respect to Fe II. It may also be that Fe II is blueshifted with respect to Mg II; however, we cannot distinguish between these cases. Kovačević-Dojčinović & Popović (2015) in their study observed redshifts, not blueshifts of the Fe II. In addition, the conclusion about the relative shift strongly depends on the combination of the Fe II template used and the adopted redshift, as we discuss in Appendix C.

Unfortunately, we are unable to establish the proper position of the rest frame for our SALT observation. We failed to identify the narrow [NeV]3426.85 Å line, which is relatively strong in the quasar spectra,[12] but this search did not yield a reliable identification.

3.2. Determination of the Mean and RMS Spectra

For constructing the mean and the rms spectra, we follow the standard procedure as explained by Peterson et al. (2004). The mean spectrum is calculated using the following relation

$$\overline{F(\lambda)} = \frac{1}{N}\sum_{i=1}^{N} F_i(\lambda), \qquad (2)$$
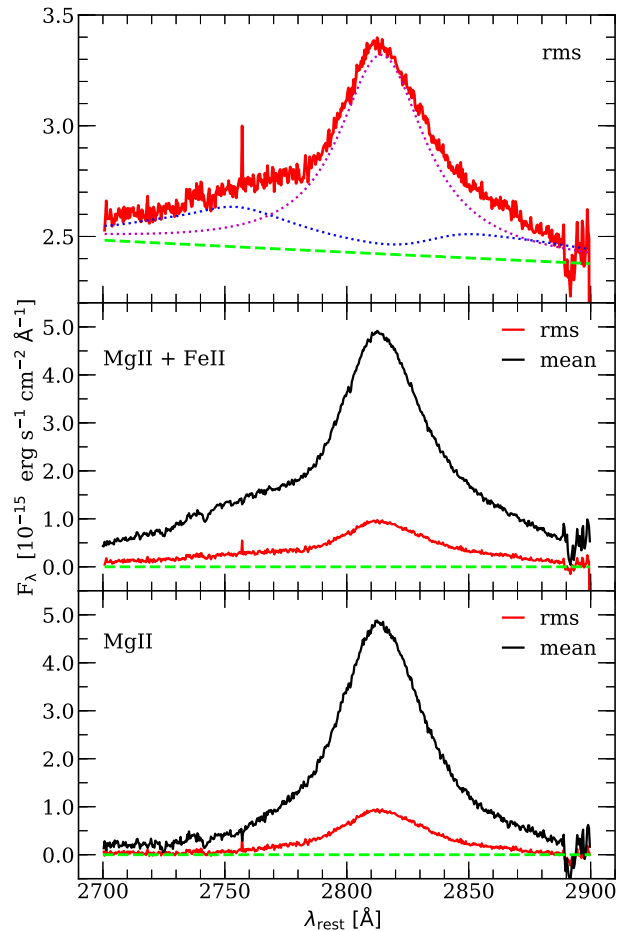
Figure 2. Decomposition of the flux-calibrated rms spectrum (top panel) and the comparison of the rms (red) and mean (black) spectra at the zero-flux level (represented by a dashed green line), first with the continuum subtracted (Mg II +Fe II; middle panel), and subsequently with the Fe II emission subtracted (Mg II; bottom panel). From the rms spectra it is clear that the core of Mg II line is the most variable, with a much smaller variability in the wings.

where $F_i(\lambda)$ are individual spectra. For studying variability phenomena, we also construct an rms spectrum using

$$S(\lambda) = \left\{\frac{1}{N-1}\sum_{i=1}^{N}[F_i(\lambda) - \overline{F(\lambda)}]^2\right\}^{1/2}. \qquad (3)$$

The flux-calibrated mean and rms spectra are shown in the top panels of Figures 1 and 2, respectively. For the flux calibration we used the composite quasar spectra created by Vanden Berk et al. (2001). For the continuum, they proposed a power law with an index of $\alpha_\lambda = -1.56$. This continuum was normalized for each spectrum according to the V magnitudes reported in Table A2, which were simply converted to flux units in order to get the flux normalization.

The rms spectrum was estimated following Equation (3). Mean and rms profiles look similar, but to check this more quantitatively, we fitted the rms spectrum in the same way we fitted the mean spectrum. The result is shown in Figure 2, upper panel. The line is still well fitted when we use a single Lorentzian model. The FWHM in rms spectrum is 4337 km s^{-1}, only marginally narrower than the FWHM of the mean spectrum (4380 km s^{-1}). When the mean and rms spectra are compared at the zero-flux level, i.e., with the continuum subtracted, we see that the core of Mg II is most variable, with

the wings having a much smaller variability, which could be attributed to Fe II emission (see the central panel of Figure 2). If we subtract the Fe II pseudo-continuum from the rms and mean spectra, the only variable part of the Mg II emission is at the core of the line (see the bottom panel of Figure 2). The EW(Mg II) if measured in the rms spectrum is 21.01 Å, lower than in the mean spectrum (27.45 Å), and EW(Fe II) is lower than in the mean spectrum (8.32 Å instead of 10.13 Å), which results from the enhanced role of the continuum power law. The consistency of the rms and the mean spectra fits also supports the single-component Lorentzian fit of the line shape.

3.3. Spectral Fits of Individual Observations

For each of the spectra, the EW(Mg II), FWHM(Mg II), EW(Fe II), shift between Mg II and Fe II, and power spectrum parameters were determined. The results are given in Table A1, and Figure 3 visually shows the evolution of these properties with time.

The mean shift of the Mg II and Fe II lines, calculated from the individual spectra, is 1582 km s^{-1}, somewhat smaller than obtained from the mean spectrum. Variations from one spectrum to the other are at the level of 82 km s^{-1} (dispersion), larger than individual errors. If we fit a linear trend, we see a systematic increase of the Mg II and Fe II separation by 109 km s^{-1} in six years, but it is not much larger than the dispersion in the measurements; however, it seems formally significant if we use the individual measurement errors given in Table A1. The corresponding acceleration 18 km s^{-1} yr^{-1} is much smaller than the large value of 104 ± 14 km s^{-1}yr^{-1} found for the quasar HE 0435-4312 also using the SALT instrument (Średzińska et al. 2017).

The averaged FWHM is 4390.8 km s^{-1}; the dispersion is 200 km s^{-1}, again slightly larger than typical measurement error, but no interesting trends could be noticed. Thus, we observe some small variations in the line shape, but they are indeed marginal, consistent with the fact that rms spectrum is similar to the mean shape of the line.

3.4. Lightcurves: Variability and Linear Trends

The continuum photometric lightcurve and the Mg II light-curve are presented in Figure 3. The continuum shows a mostly slow but noticeable variation. A single brightening trend dominates for most of the monitoring period, replaced with some dimming during the last 1.5 yr. The overall variability level of the continuum is $F_{\rm var} = 13.0\%$, if BMT telescope is included, and 10.4%, if these data are not taken into account. Here we use the standard definition of the excess variance,

$$F_{\rm var} = \sum_{i=1}^{N} \frac{(x_i - \bar{x})^2 - \delta x_i^2}{N\bar{x}^2}, \qquad (4)$$

where $\bar{x}$ is the average value, and δx_i is the individual measurement error. Because this linear trend seems suggestive, we also checked the shorter timescale variability by first fitting a linear trend to the lightcurve in the log space (i.e., when using magnitudes), and then subtracting this trend from the original lightcurve. We did this only for the data without BMT. The $F_{\rm var}$ dropped from 10.4% down to 7.4%.

The Mg II line variability is lower, $F_{\rm var} = 7.2\%$, and $F_{\rm var} = 7.1\%$, depending on whether BMT telescope data were or were not used for Mg II calibration, respectively. It is
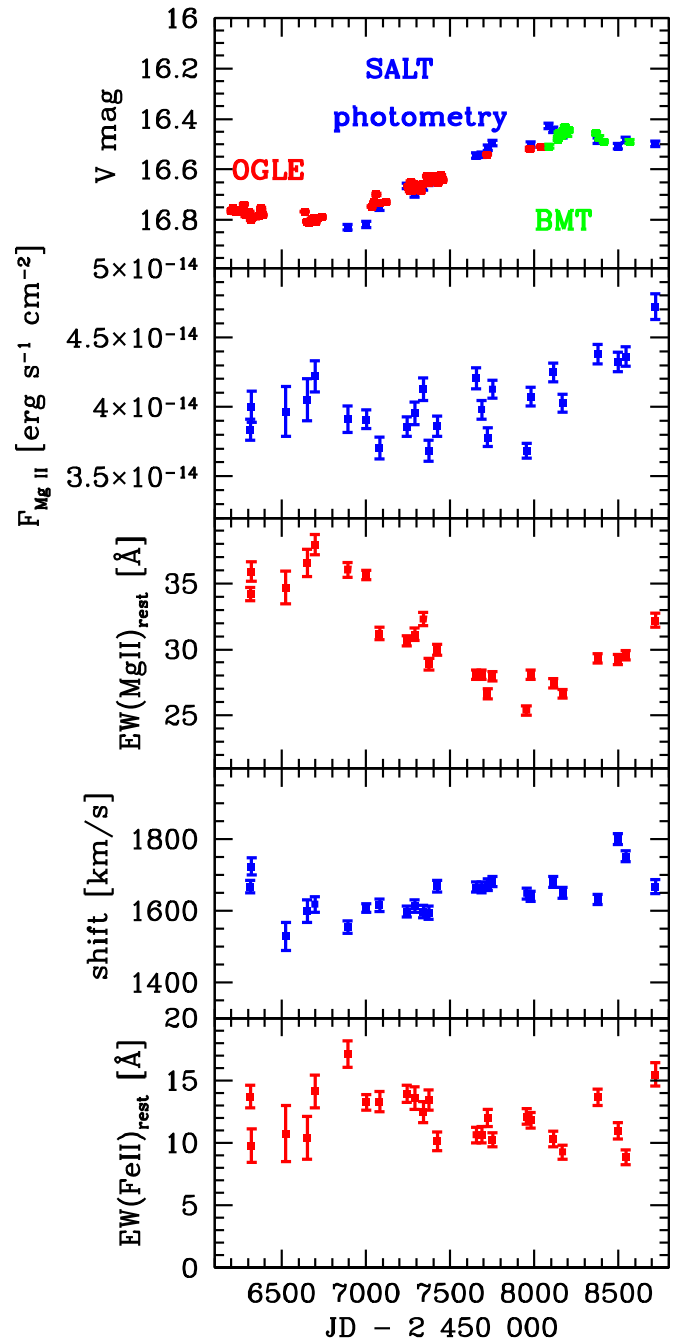
Figure 3. Temporal evolution of photometric and spectroscopic characteristics from the monitoring of the quasar HE 0413-4031. From the top to the bottom panels: photometric lightcurve (V-band magnitude) from OGLE, SALT, and BMT (color-coded; BMT data were shifted by 0.171 mag up to correct for the systematic offset with respect to the OGLE data); Mg II line-emission lightcurve (in erg s^{-1} cm^{-2}); the equivalent width of the Mg II line in Å; the velocity shift of the Mg II line with respect to the Fe II line in km s^{-1}; the equivalent width of Fe II line in Å. The time is expressed in JD-2450000.

interesting to note, however, that the levels of variability in Mg II and the continuum are comparable if the long-term trend was subtracted from the data.

We also determine Fe II lightcurve, and the variability level of Fe II seems higher, at the level of 14.7% if BMT data are neglected, and 14.9% if the BMT data are included. However, the measurement errors are large due to the coupling between the continuum and Fe II pseudo-continuum.
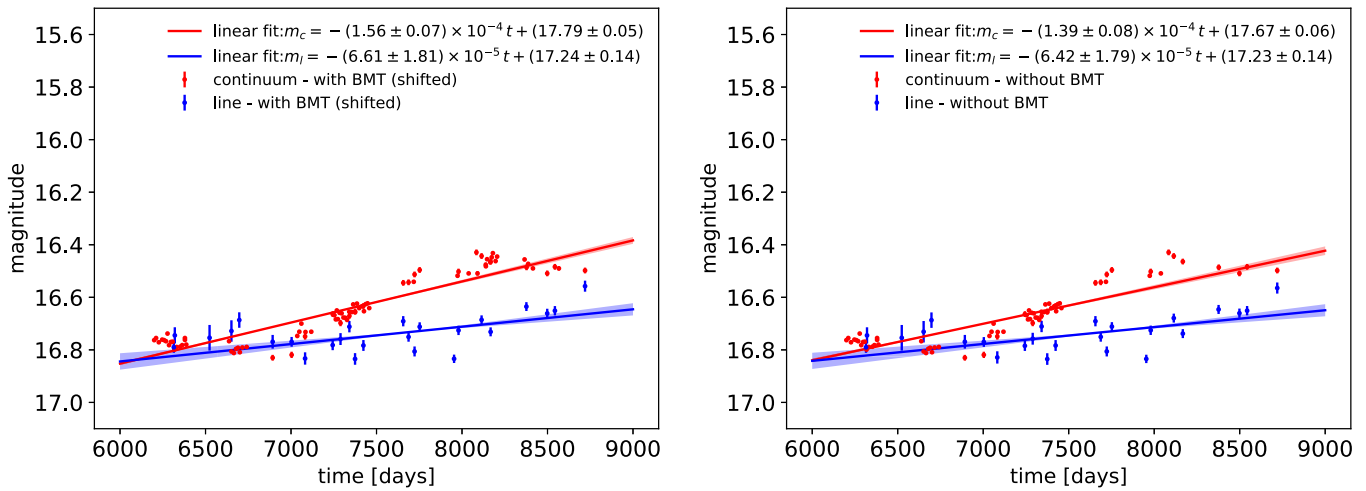
Figure 4. Linear-trend fit to both continuum and line-emission lightcurves in the log space. Left panel: the linear trend fits with BMT data included. The BMT data were shifted by 0.171 mag to correct for the systematic shift with respect to the OGLE data. The legend includes the best-fit parameters for both the continuum and the line-emission lightcurves. The fit statistics are $\chi^2 = 7121.4$ and $\chi^2_{\rm red} = 84.8$ for the continuum and $\chi^2 = 177.9$ and $\chi^2_{\rm red} = 7.7$ for the line lightcurve. Right panel: as in the left panel, but without BMT data. The fit statistics are $\chi^2 = 5609.2$ and $\chi^2_{\rm red} = 79.0$ for the continuum and $\chi^2 = 172.9$ and $\chi^2_{\rm red} = 7.5$ for the line lightcurve.

The mean monochromatic luminosity at 3000 Å can be derived from the V-band magnitude of 16.5, using the extinction reported in NED with a value of 0.034, source redshift of 1.389, and standard cosmological parameters for the flat universe ($H_0 = 70 \, {\rm km \, s^{-1} \, Mpc^{-1}}$, $\Omega_{\rm m} = 0.28$, and $\Omega_\Lambda = 0.72$, see Kozłowski 2015, for details). We obtain $\log L_{3000} = 46.754$. The uncertainty of the monochromatic luminosity can be estimated from the minimum and the maximum points along the photometric lightcurve, 16.429 mag and 16.830 mag, respectively, which implies $\log L_{3000}^{\rm max} = 46.782$ and $\log L_{3000}^{\rm min} = 46.622$. Hence, for the further analysis, we consider $\log L_{3000} = 46.754^{+0.028}_{-0.132}$.

As already pointed out, the linear trend is present in both continuum and Mg II line emission lightcurves. In Figure 4, we show the fit of a linear function to both lightcurves, considering the case with and without BMT data in the left and right panels, respectively. The linear trend is toward smaller magnitudes, i.e., the continuum and line-emission flux densities increase during the observational run. The slope of the linear trend is larger for the continuum than for the line-emission lightcurves. The continuum slope is $s_{\rm c} = 0.057 \, {\rm mag \, yr^{-1}}$ and the line slope is $s_{\rm l} = 0.024 \, {\rm mag \, yr^{-1}}$ with the BMT data included; without BMT data, the continuum increase drops a little, $s_{\rm c} = 0.051 \, {\rm mag \, yr^{-1}}$, while the line-emission slope is comparable, $s_{\rm l} = 0.023 \, {\rm mag \, yr^{-1}}$. In other words, the decrease in the continuum magnitude is 2.38 and 2.17 larger than the decrease for the line-emission magnitude with and without BMT data, respectively.

4. Results: Time-delay Determination

As for the intermediate-redshift quasar CTS C30.10 ($z = 0.90052$) (Czerny et al. 2019), we apply several methods to determine the time-delay between the continuum V band and Mg II line emission. Apart from the standard interpolated cross-correlation function, we apply several statistically robust methods suitable for unevenly sampled, heterogeneous pairs of lightcurves (see Zajaček et al. 2019b, for an overview), namely the discrete correlation function, z-transformed discrete correlation function, JAVELIN, χ^2 method, Von Neumann, and Bartels estimator. For all seven methods, we consider the two pairs of lightcurves, those with and without magnitude-

shifted BMT data. The detailed description of the time-delay analysis is in the Appendix in Section B, with subsections B.1–B.6 describing individual methods including the corresponding plots and the tables.

4.1. Final Time-delay for Mg II Line

Due to the systematic offset of the BMT data in the continuum lightcurve, we decided to distinguish two cases for all time-delay analysis techniques. For a matter of completeness, below we summarize in Table 1 the main results for all the methods, including the cases with and without magnitude-shifted BMT data. The most prominent peak in the time-delay distributions is the peak close to 700 days in the observer's frame. This peak is generally present in all seven methods. However, the ICCF analysis generally gives longer time-delays of 900–1000 days, which could be caused by the interpolation and hence by adding new points to the analysis. A noticeable difference is also for the JAVELIN method, where the time-delay peak is close to 1050 days. Because JAVELIN uses the damped random walk for fitting the continuum lightcurve, which is then smoothed and time-delayed to reproduce the Mg II line-emission lightcurve, extra points are introduced to the lightcurves in a similar way as for the ICCF. This can lead to biases and artifacts, especially for irregular and sparse data sets. This is why we decided to prefer the peak around 700 days, which is the most prominent for all discrete methods that do not require interpolation and are model-independent (DCF, zDCF, Von Neumann). The detected time-delay of $498.9^{+170.9}_{-125.9}$ days for the Von Neumann estimator with shifted BMT data is most likely an artifact because it is an excess given by only one point; see Figure B6 (left panel). The second minimum of the Von Neumann estimator around 700 days is then more pronounced and clearly given by more points. In addition, the minimum around 500 days is not present for the case without BMT data; see Figure B6 (right panel).

Given the arguments above, we focus on the observed time-delay around 700 days. Concerning the average value, we obtain the rest-frame time-delay of $\tau_1 = 302.2^{+43.3}_{-61.4}$ days for the case with the shifted BMT data, and $\tau_2 = 303.0^{+37.8}_{-24.5}$ days for the case without them. The final average value then is

Table 1
Summary List of the Time-delays Expressed in Light Days in the Observer's Frame between the Continuum and Mg II Line-emission Lightcurves for the Flat-spectrum Radio Quasar HE 0413-4031

Method	With Shifted BMT data	Without BMT data
ICCF interpolated continuum—centroid [days]	$1004.6^{+196.8}_{-246.2}$	$1003.2^{+205.3}_{-235.4}$
ICCF interpolated line—centroid [days]	$1008.4^{+142.2}_{-276.9}$	$1034.171^{+139.1}_{-248.9}$
ICCF symmetric—centroid [days]	$1009.7^{+113.6}_{-211.5}$	$1021.7^{+114.5}_{-207.8}$
DCF peak time-delay—bootstrap [days]	$720.4^{+115.1}_{-147.9}$	$726.0^{+114.4}_{-145.7}$
zDCF maximum likelihood	$720.9^{+323.9}_{-527.3}$	$720.9^{+331.3}_{-100.1}$
JAVELIN peak time-delay [days]	$1053.7^{+79.8}_{-163.6}$	$1058.5^{+77.1}_{-150.7}$
Von Neumann peak—bootstrap [days]	$498.9^{+170.9}_{-125.9}$	$711.3^{+149.0}_{-139.5}$
Bartels peak—bootstrap [days]	$710.9^{+172.3}_{-173.0}$	$714.6^{+176.1}_{-164.6}$
χ^2 peak—bootstrap [days]	$720.4^{+145.6}_{-102.2}$	$727.7^{+160.0}_{-85.2}$
Average of the most frequent peak—observer's frame [days]	$718.2^{+102.8}_{-145.8}$	$720.1^{+89.8}_{-58.3}$
Average of the most frequent peak—rest frame	$302.2^{+43.3}_{-61.4}$	$303.0^{+37.8}_{-24.5}$
Average of the secondary peak—observer's frame [days]	$1019.1^{+69.9}_{-114.2}$	$1029.4^{+71.0}_{-107.2}$
Average of the secondary peak—rest frame [days]	$428.8^{+29.4}_{-48.1}$	$433.2^{+29.9}_{-45.0}$

Note. We distinguish for all methods two cases—with and without magnitude-shifted BMT data.

$\overline{\tau} = 302.6^{+28.7}_{-33.1}$ days, which corresponds to the light-travel distance of $R_{\rm Mg\,II} = c\overline{\tau} = 0.254^{+0.024}_{-0.028}$ pc $\sim 10^{17.9}$ cm. The inferred value of the light-travel distance $R_{\rm Mg\,II}$ is larger than typical BLR length-scales inferred from other RM campaigns with time-delays of the order 10–100 light days for AGN with a broad range of black hole masses (Korista & Goad 2000, 2004; Shen et al. 2016). The length-scale of the BLR has implications for the line variability, as was shown by Guo et al. (2020), and we will specifically discuss the Mg II line–continuum variability relation in Section 6.2.

The results provided by the ICCF and the JAVELIN analyses provide a time-delay that we treat as secondary for the reasons of interpolation and the model-dependence. In the rest frame, this secondary time-delay is $428.8^{+29.4}_{-48.1}$ days for the case with the shifted BMT data and $433.2^{+29.9}_{-45.0}$ days for the case without the BMT data. The average rest-frame value is $431.0^{+21.0}_{-32.9}$ days. This secondary time-delay peak should be reevaluated when more continuum and line-emission data are available to assess if it is just an artifact of data sampling irregularity.

5. Results: Mg II–based Radius–Luminosity Relation

5.1. Preliminary Virial Black Hole Mass and Eddington Ratio

The virial black hole mass can be determined from the virial relation for the BLR, $M_{\bullet} = f_{\rm vir}\,c\tau_{\rm BLR}\,{\rm FWHM}^2/G = (1.134^{+0.089}_{-0.072}) \times 10^9\,M_{\odot}$, which was calculated assuming the virial factor equal to unity, the average time-delay for Mg II inferred earlier, and the best-fit FWHM of 4380^{+14}_{-15} km s^{-1}. In general, however, the virial factor may deviate from unity, which is indicated by the study of Mejía-Restrepo et al. (2018), which implies the anticorrelation between the virial factor and the line FWHM, which is in our case the main source of uncertainty. According to Mejía-Restrepo et al. (2018), we have

$$f_{\rm vir,Mg\,II} = \left(\frac{{\rm FWHM}_{\rm obs}({\rm Mg\,II})}{3200 \pm 800\,{\rm km\,s}^{-1}} \right)^{-1.21 \pm 0.24}, \qquad (5)$$

which for FWHM $= 4380^{+14}_{-15}$ km s^{-1} leads to the virial factor less than unity, $f_{\rm vir,Mg\,II} = 0.42$–$0.92$, and the virial black hole

mass in the range of $M_{\bullet} = 4.8 \times 10^8$–$1.0 \times 10^9\,M_{\odot}$, hence we have a factor of 2 uncertainty in the virial black hole mass. The Eddington luminosity can be estimated as

$$L_{\rm Edd} = 1.256 \times 10^{47} \left(\frac{M_{\bullet}}{10^9\,M_{\odot}} \right) {\rm erg\,s}^{-1}, \qquad (6)$$

while the bolometric luminosity may be calculated using the bolometric correction with respect to $\lambda = 3000$ Å, $L_{\rm bol} = (5.62 \pm 1.14)L_{3000}$ (Richards et al. 2006), which leads to the Eddington ratio of $\eta_{\rm Edd} = L_{\rm bol}/L_{\rm Edd} \approx 2.18$. Using the power-law calibration of the bolometric correction by Netzer (2019), we obtain $L_{\rm bol} \simeq 2.8L_{3000}$, which gives $\eta_{\rm Edd} \approx 1.27$. Hence, these values imply close to the Eddington or even the super-Eddington accretion mode.

5.2. Position in the Radius–Luminosity Plane

By combining the rest-frame time-delay and the monochromatic luminosity of HE 0413-4031, we can position the source on the radius–luminosity plane alongside the other quasars to check for the potential deviation of HE 0413-4031 due to its high accretion rate, as was previously detected for super-Eddington sources monitored in the broad Hβ line (Wang et al. 2014a, 2014b; Martínez-Aldama et al. 2019).

With the rest-frame time-delay of $\overline{\tau} = 302.6^{+28.7}_{-33.1}$ days and the monochromatic luminosity of $\log L_{3000} = 46.754^{+0.028}_{-0.132}$, the source HE 0413-4031 lies below the expected radius–luminosity relation, $R({\rm Mg\,II}) - L_{3000}$ (Vestergaard & Osmer 2009). We demonstrate this in Figure 5, in which we compiled all the sources whose time-delay was determined for the Mg II line (10 sources, see Table 3 in Czerny et al. 2019), including CTS C30.10 and the new source HE 0413-4031. The list of all the sources with measured time-delays and determined monochromatic luminosities is in Table 2. With a large scatter ($\sigma = 0.246$ dex), the sources approximately follow the radius–luminosity relationship previously derived for the
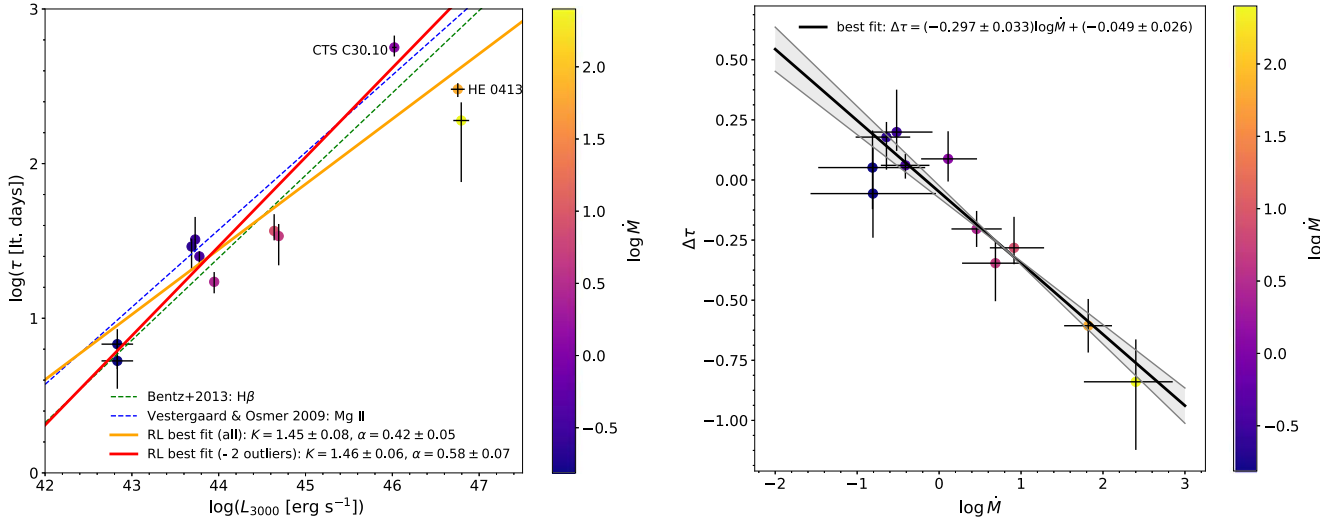
Figure 5. Radius–luminosity relation for the reverberation-mapped sources in the broad Mg II line resembles the radius–luminosity relation for the Hβ line. Left panel: radius–luminosity relation for the RM quasars monitored in the broad Mg II line. Clearly, the sources follow within uncertainties the scaling relationship previously derived by Vestergaard & Osmer (2009) for the Mg II line (dashed blue line) as well as the Hβ radius–luminosity relationship of Bentz et al. (2013) (dashed green line). The best-fit relationships are also displayed, both for the case when all the sources are included in the fitting procedure (solid orange line) and for the case when two outliers that are below the radius–luminosity relations are removed (CTS252 and HE 0413-4031) toward the higher luminosities (solid red line). Individual sources are color-coded to show the logarithm of the dimensionless accretion-rate parameter $\dot{M}$ (see Equation (11)), according to the color bar to the right. Right panel: the strong anticorrelation (with the Pearson correlation coefficient of $p = -0.940$) of the parameter $\Delta\tau$, which expresses the rate of departure from the radius–luminosity relation (see also Equation (12)), with respect to the dimensionless accretion-rate parameter $\dot{M}$ expressed by Equation (11).

Table 2
Characteristics of Reverberation-mapped Sources Monitored Using the Broad Mg II Line

Source	z	τ (days)	$\log (L_{3000}(\mathrm{erg\ s^{-1}}))$	FWHM (Mg II) (km s^{-1})	$\dot{M}$	$\Delta\tau$	τ_{corr} (days)
141214.20+532546.7[1,2]	0.45810	$36.7^{+10.4}_{-4.8}$	44.63882 ± 0.00043	2391 ± 46	$8.21^{+6.94}_{-5.58}$	$-0.28^{+0.13}_{-0.07}$	$80.7^{+22.9}_{-10.6}$
141018.04+532937.5[1,2]	0.46960	$32.3^{+12.9}_{-5.3}$	43.7288 ± 0.0051	3101 ± 76	$0.30^{+0.31}_{-0.21}$	$0.20^{+0.18}_{-0.08}$	$27.1^{+10.8}_{-4.4}$
141417.13+515722.6[1,2]	0.60370	$29.1^{+3.6}_{-8.8}$	43.6874 ± 0.0029	3874 ± 86	$0.23^{+0.15}_{-0.20}$	$0.18^{+0.06}_{-0.14}$	$22.4^{+2.8}_{-6.8}$
142049.28+521053.3[1,2]	0.75100	$34.0^{+6.7}_{-12.0}$	44.6909 ± 0.0009	4108 ± 39	$4.87^{+3.57}_{-4.57}$	$-0.35^{+0.09}_{-0.16}$	$64.2^{+12.6}_{-22.6}$
141650.93+535157.0[1,2]	0.52660	$25.1^{+2.0}_{-2.6}$	43.778 ± 0.002	4066 ± 202	$0.39^{+0.26}_{-0.27}$	$0.06^{+0.05}_{-0.06}$	$22.6^{+1.8}_{-2.3}$
141644.17+532556.1[1,2]	0.42530	$17.2^{+2.7}_{-2.7}$	43.9480 ± 0.0011	2681 ± 96	$2.87^{+2.03}_{-2.03}$	$-0.20^{+0.07}_{-0.07}$	$27.8^{+4.4}_{-4.4}$
CTS252[3,4]	1.89000	$190.0^{+59.0}_{-114.0}$	46.79 ± 0.09	3800 ± 380	$251.55^{+261.03}_{-367.22}$	$-0.84^{+0.18}_{-2.03}$	$1136.2^{+353.1}_{-682.0}$
NGC4151[5,6]	0.00332	$6.8^{+1.7}_{-2.1}$	42.83 ± 0.18	4823 ± 1105	$0.15^{+0.23}_{-0.23}$	$0.05^{+0.15}_{-0.17}$	$4.7^{+1.2}_{-1.4}$
NGC4151[5,6]	0.00332	$5.3^{+1.9}_{-1.8}$	42.83 ± 0.18	6558 ± 1850	$0.16^{+0.28}_{-0.27}$	$-0.06^{0.19}_{-0.18}$	$3.7^{+1.3}_{-1.2}$
CTS C30.10[7,7]	0.90052	564^{+109}_{-71}	46.023 ± 0.026	5009 ± 325	$1.29^{+1.05}_{-0.98}$	$+0.09^{+0.11}_{-0.09}$	$721.4^{+139.4}_{-90.8}$
HE 0413-4031[8,9]	1.37648	$302.6^{+28.7}_{-33.1}$	46.754 ± 0.080	4380 ± 14	$66.04^{+44.17}_{-44.76}$	$-0.61^{+0.11}_{-0.11}$	$1223.9^{+116.4}_{-134.1}$

Note. From the left to the right column, the table lists the source name, redshift, measured time-delay in light days in the rest frame, the logarithm of the monochromatic luminosity at 3000 Å, FWHM of Mg II in km s^{-1}, the dimensionless accretion rate as defined in Equation (11), departure parameter $\Delta\tau$ defined by Equation (12), and the corrected time-delay expressed in light days in the rest frame (see also Equation (14)). The superscripts to source names indicate the sources, from which we obtained the measured time-delay (first source) and the monochromatic luminosity at 3000 Å (second source): (1) Shen et al. (2016); (2) Shen et al. (2019); (3) Lira et al. (2018); (4) NED, NUV, *GALEX*; (5) Metzroth et al. (2006); (6) Code & Welch (1982); (7) Czerny et al. (2019); (8) this work; and (9) a script of Kozłowski et al. (2010).

Mg II line (Vestergaard & Osmer 2009),

$$\log\left[\frac{\tau(\mathrm{Mg\ II})}{1\mathrm{lt\text{-}day}}\right] = 1.572 + 0.5\log\left(\frac{L_{3000}}{10^{44}\ \mathrm{erg\ s^{-1}}}\right), \quad (7)$$

as well as the radius–luminosity relationship derived for the Hβ line for lower-redshift sources by Bentz et al. (2013),

$$\log\left[\frac{\tau(\mathrm{H}\beta)}{1\mathrm{lt\text{-}day}}\right] = 1.391 + 0.533\log\left(\frac{L_{3000}}{10^{44}\ \mathrm{erg\ s^{-1}}}\right), \quad (8)$$

in which we replaced L_{5100} monochromatic luminosity by L_{3000} using $L_{5100} \simeq 0.556 L_{3000}$, using the power-law relations for

the bolometric corrections derived by Netzer (2019). The scatter of the sources around the relation by Bentz et al. (2013) is $\sigma = 0.269$ dex, which is comparable to the scatter with respect to the relation by Vestergaard & Osmer (2009).

We also fitted the general radius–luminosity relationship $\log(\tau/1\ \mathrm{lt\text{-}day}) = K + \alpha\log(L_{3000}/10^{44}\ \mathrm{erg\ s^{-1}})$ to all available data. We obtained the best-fit parameters of $K = 1.45 \pm 0.08$ and $\alpha = 0.42 \pm 0.05$ with $\chi^2 = 76.6$ and $\chi^2_{\mathrm{red}} = 8.5$. Subsequently, we removed 2 outliers—CTS252 and HE 0413-4031—that are significantly below RL relations in Equation (7) and Equation (8). This helped to improve the fit, with the best fit with $\chi^2 = 36.7$ and $\chi^2_{\mathrm{red}} = 5.2$, and the

final relation based on Mg II data can be expressed as

$$\log\left[\frac{\tau(\text{Mg II})}{1\text{lt-day}}\right] = (1.46 \pm 0.06) + (0.58 \pm 0.07)$$
$$\times \log\left(\frac{L_{3000}}{10^{44}\,\text{erg s}^{-1}}\right). \quad (9)$$

Both best-fit relations are depicted in Figure 5 with solid lines.

The time-delay offset can be explained by the higher accretion rate implied by the super-Eddington luminosity. The correlation of the time-delay offset with the accretion rate was shown previously for reverberation-mapped sources in the Hβ line (Du et al. 2018; Martínez-Aldama et al. 2019), and we will demonstrate it in the following section for the broad Mg II line. By moving the source HE 0413-4031 back onto the radius–luminosity relation, we can estimate the corrected black hole mass using (Vestergaard & Osmer 2009)

$$M_\bullet^{\text{Mg II}} = 10^{zp(\lambda)}\left[\frac{\text{FWHM(Mg II)}}{1000\,\text{km s}^{-1}}\right]^2\left(\frac{\lambda L_\lambda}{10^{44}\,\text{erg s}^{-1}}\right)^{0.5}, \quad (10)$$

which for FWHM(Mg II) = 4380^{+14}_{-15} km s^{-1} and $zp(\lambda) = 6.86$ ($\lambda = 3000\,\text{Å}$) yields $M_\bullet^{\text{Mg II}} = 3.31 \times 10^9\,M_\odot$ using the monochromatic luminosity of $\log L_{3000} = 46.754$.

Hence, the black hole mass obtained from the radius–luminosity relation is larger by a factor of at least $\sim$3 than the maximum mass inferred from the RM time-delay, taking into account the uncertainty in the virial factor. The Eddington ratio for the higher mass then drops to $\eta_{\text{Edd}} = 0.77$ for the constant bolometric correction factor of BC = 5.62 (Richards et al. 2006). For the more precise luminosity-dependent bolometric correction of BC = $25 \times (L_{3000}/10^{42}\,\text{erg s}^{-1})^{-0.2} = 2.80$ for $L_{3000} = 10^{46.754}\,\text{erg s}^{-1}$ (Netzer 2019), we get an even smaller Eddington ratio of $\eta_{\text{Edd}} = 0.38$, which is also consistent with the SED fitting presented in Section 6.3.

5.3. Correction of the Accretion-rate Effect along the Radius–Luminosity Relation

In the optical range, it has been observed that the accretion rate is responsible for the departure of the radius–luminosity relation more than the intrinsic scatter. Du et al. (2018, and references therein) showed that the sources with the highest accretion rates have time-delays shorter than expected from the optical radius–luminosity relation. However, the accretion-rate effect can be corrected, recovering the standard results (Martínez-Aldama et al. 2019). Following this idea, we repeated the same exercise for all Mg II reverberation-mapped data (see Table 2).

The black hole mass was estimated assuming a virial factor anticorrelated with the FWHM of the emission line (Equation (5)), which apparently corrects the orientation effect to a certain extent. Because the Eddington ratio has shown a large scatter in comparison with other expressions of the accretion rate (Martínez-Aldama et al. 2019), we will use the dimensionless accretion rate (Du et al. 2016),

$$\dot{M} = 20.1\left(\frac{l_{44}}{\cos\theta}\right)^{3/2}m_7^{-2}, \quad (11)$$

where l_{44} is the luminosity at 3000 Å in units of 10^{44} erg s^{-1}, $\theta = 0.75$ is the inclination angle of disk to the line of sight, and m_7 is the black hole mass in units of $10^7\,M_\odot$. In Figure 5 (left
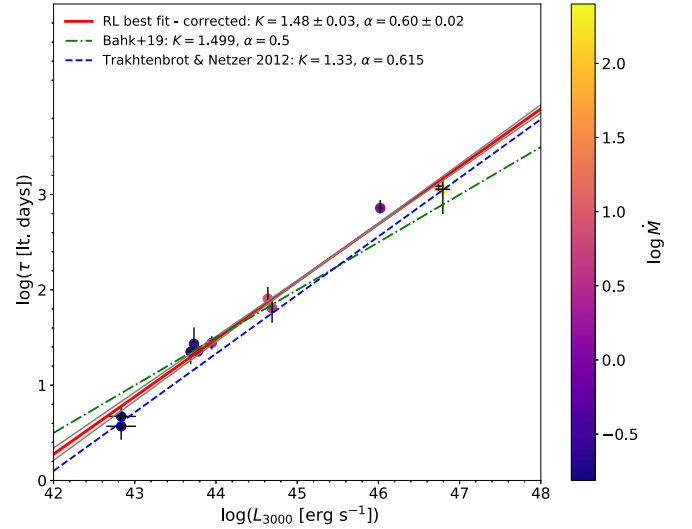

Figure 6. The radius–luminosity relation for the Mg II broad-emission line; the rest-frame time-delays were corrected for the accretion-rate effect. The best-fit linear relation in the log space is $\log(\tau/1\text{ lt. day}) = (1.48 \pm 0.03) + (0.60 \pm 0.02)\log(L_{3000}/10^{44}\text{ erg s}^{-1})$, with $\chi^2 = 11.40$ and $\chi^2_{\text{red}} = 1.27$. For comparison, we also show the radius–luminosity relation as inferred by Bahk et al. (2019), which has the same normalization factor as our relation, but a smaller slope of 0.5. In addition, we depict the radius–luminosity relation constructed by Trakhtenbrot & Netzer (2012), which, on the other hand, has a comparable slope of $\alpha = 0.615$, but a smaller normalization factor of $K = 1.33$.

panel), we show the variation of the dimensionless accretion rate along the radius–luminosity relation, which is similar to the observed one in the optical range.

To estimate the departure from the radius–luminosity relation, we use the parameter $\Delta\tau$, which is simply the difference between the observed time-delay and the expected one from the radius–luminosity relation,

$$\Delta\tau = \log\left(\frac{\tau_{\text{obs}}}{\tau_{\text{R–L}}}\right). \quad (12)$$

We estimate $\tau_{\text{R–L}}$ from the radius–luminosity relation described in Equation (9). Values are reported in Table 2. The largest departure from the radius–luminosity relation is associated with the highest accretion-rate sources, which is clearly evidenced in Figure 5 (right panel). The Pearson coefficient ($p = -0.940$) also indicates a strong anticorrelation between $\Delta\tau$ and $\dot{M}$. Performing a linear fit, we get the relation

$$\Delta\tau(\dot{M}) = (-0.297 \pm 0.033)\log\dot{M} + (-0.049 \pm 0.026), \quad (13)$$

for which $\chi^2 = 6.75$ and $\chi^2_{\text{red}} = 0.75$. This expression can be used to recover the expected values from the radius–luminosity relation using the relation

$$\tau_{\text{corr}}(\dot{M}) = 10^{-\Delta\tau(\dot{M})} \cdot \tau_{\text{obs}}. \quad (14)$$

The corrected rest-frame time-delays are listed in Table 2. Based on them, we construct a new version of the radius–luminosity relation for the Mg II line corrected for the accretion-rate effect (see Figure 6). It shows a smaller scatter of $\sigma = 0.104$ dex in comparison with the radius–luminosity relation before the correction, which is $\sigma = 0.221$ dex when all the sources are included and $\sigma = 0.186$ dex with two outliers

removed. The best-fit linear relation has smaller uncertainties with $\chi^2 = 11.40$ and $\chi^2_{\rm red} = 1.27$ and can be expressed as

$$\log\left[\frac{\tau({\rm Mg\,II})}{1{\rm lt\text{-}day}}\right] = (1.48 \pm 0.03) + (0.60 \pm 0.02)$$
$$\times \log\left(\frac{L_{3000}}{10^{44}\ {\rm erg\ s^{-1}}}\right). \quad (15)$$

The dispersion around the new relation is very small, equal to 0.104 dex. This is smaller than the dispersion of 0.13 dex in the original radius–luminosity relation of Bentz et al. (2013) after an artificial removal of outliers, despite the fact that the Mg II relation covers a broad range of the luminosities, redshifts, and Eddington ratios. It is not clear at this point whether the smaller dispersion is a property of the Mg II emission or it just results from the fact that the Mg II data do not come from so many different monitoring campaigns.

The normalization coefficient in Equation (15) is within uncertainties consistent with the normalization factor inferred from the Mg II–based black hole mass estimator by Bahk et al. (2019),

$$\log\left[\frac{\tau({\rm Mg\,II})}{1{\rm lt\text{-}day}}\right] \simeq 1.499 + 0.5 \log\left(\frac{L_{3000}}{10^{44}\ {\rm erg\ s^{-1}}}\right), \quad (16)$$

where we adopted their fitting Scheme 4 and assumed the virial factor $f_{\rm vir} \equiv 1$ while transforming $M_\bullet \propto L_{3000}^{0.5}(\Delta V)^2$ relation to $\tau \propto L_{3000}^{0.5}$ relation. The relation 16 is also shown in Figure 6 for comparison with our best-fit relation 15.

However, the best-fit slope is larger than the slope of 0.5 in Equation (16), which is also expected from the simple photoionization arguments. Currently, this may be just a systematic effect due to a small number of reverberation-mapped sources using the Mg II line. The larger slope currently yields a significantly small scatter, because for the relation given by Equation (16) the scatter is $\sigma = 0.187$ dex for the corrected time-delays. For the uncorrected rest-frame time-delays, the scatter is $\sigma = 0.247$ dex and $\sigma = 0.189$ for the whole Mg II sample (sources in Table 2) and the Mg II sample without the two outliers (CTS252 and HE 0413-4031), respectively.

On the other hand, our best-fit slope is very similar to the value of $\alpha = 0.615$ inferred by Trakhtenbrot & Netzer (2012), who, on the other hand, have a smaller normalization factor $K = 1.33$. Our slope value is also located between the slopes derived for the $\tau({\rm Mg\,II})$–L_{3000} relation by McLure & Jarvis (2002) ($\alpha = 0.47$) and by McLure & Dunlop (2004) ($\alpha = 0.62$). However, all of the above-mentioned Mg II–based radius–luminosity relations were calibrated based on the UV spectra of sources for which only Hβ line RM was performed. Certainly, more reverberation-mapped sources using the Mg II line are required to further constrain the $\tau({\rm Mg\,II})$–L_{3000} relation.

6. Discussion

Using the SALT data and the supplementary photometric monitoring, we were able to derive the time-delay of the Mg II line with respect to the continuum in $z = 1.37648$ quasar HE 0413-4031. The source is very bright in the absolute term, but the delay is formally established as $\overline{\tau} = 302.6^{+28.7}_{-33.1}$ days in the comoving frame. Although the analysis of the Mg II complex with the underlying power-law continuum and Fe II pseudo-

continuum emission is a complex task with a certain degree of degeneracy, we showed that the peak value of the time-delay distribution is not sensitive to different Fe II templates; only its uncertainty may be affected due to a different number of parameters used in each model (see also Appendix C for a detailed discussion).

This delay is shorter than derived for CTS C30.10 (Czerny et al. 2019), but similar to the delay measured for another bright quasar by Lira et al. (2018). We show that the dispersion in the measured time-delay of the Mg II line for a given range of the monochromatic flux is related to the Eddington ratio in the source, as in the Hβ time-delay (Martínez-Aldama et al. 2019), and with the appropriate correction for this effect, the dispersion around the radius–luminosity is actually very small, with $\sigma = 0.104$ dex in comparison with $\sigma = 0.221$ dex before the correction (when all the sources are included; $\sigma = 0.186$ dex with two outliers removed), which opens up a possibility for the future applications of this relation for cosmology.

In this section, we discuss more generally the validity and the accuracy of using Mg II lines in black hole mass determination. Furthermore, we show that the intrinsic Baldwin effect is present in our source, which is another way of showing that the Mg II line responds to the thermal AGN continuum. To verify if the reverberating Mg II line in our source is a reliable probe of its black hole mass, we performed a fit of the accretion disk model to the optical and UV continuum data of the source SED.

6.1. Nature of Mg II Emission

Marziani et al. (2013) showed that the FWHM of the Mg II line is systematically narrower by $\sim$20% than the Hβ line, which holds for all of its components as well as the full profile. The simple explanation is that Mg II is emitted at larger distances than Hβ from the photoionizing continuum source. The intrinsically symmetric profile of the Mg II line found in this work characterized by a one-component Lorentzian is consistent with the origin of the Mg II emission in the virialized BLR clouds, as for the Hβ broad line (Marziani et al. 2013). The Lorentzian profile may be physically explained by the turbulent motion of the emitting medium and the line broadening by its rotation (Kollatschny & Zetzl 2011; Goad et al. 2012; Kollatschny & Zetzl 2013a, 2013b). This model of the Lorentzian line profile is also consistent with the failed radiatively accelerated outflow (FRADO) model as such (Czerny & Hryniewicz 2011), in which the turbulence arises due to the failed outflow and the subsequent inflow, and the rotation is represented by the dominant Keplerian field (see also Figure 8). For Population A sources where the Mg II profile is symmetric, the Mg II gas may be considered virialized. For Population B sources, a small degree of asymmetry and the blueshift of the Mg II line may be related to outflows of the Mg II–emitting gas (Marziani et al. 2013).

Our results, in particular the studied intrinsic Baldwin effect in Section 6.2, are also consistent with the work of Yang et al. (2020), who found for the sample of 33 extreme variability quasars that the Mg II flux density responds to the variable continuum, but with a smaller amplitude. However, they also stress that the FWHM of the Mg II line does not respond to the continuum as the Balmer lines do. Therefore, black hole mass estimations based on single-epoch measurements can be luminosity-biased.

Previous works also find an overall consistency between Hβ-based and Mg II–based black hole mass estimators. Trakhtenbrot & Netzer (2012) found the scatter between these two spectral regions of 0.32 dex in terms of the black hole mass estimation, smaller than for the C IV line, for which the scatter with respect to Hβ is 0.5 dex. In addition, the same authors found that FWHM(Mg II) $\simeq$ FWHM(Hβ) up to 6000 km s^{-1}, beyond which the FWHM of Mg II seems to saturate. This is again different for the C IV line, which does not show any correlations with either the Hβ or the Mg II line. Also, the FWHM(C IV) $\lesssim$ FWHM(Hβ) for nearly half of the studied sources (see also Shen & Liu 2012, for a similar result), which contradicts RM results. Ho et al. (2012) also showed that Mg II–based black hole masses are comparable within uncertainties to those based on Hα, while C IV–based mass estimates differed by as much as a factor of 5. Hence, the usage of the broad Mg II line for black hole mass estimating is justified for sufficiently large samples, while C IV should not be applied as a reliable virial black hole mass estimator. This is in line with the overall picture, where low-ionization lines (Hα, Hβ, Mg II) originate in the bound line-emitting, photoionized clouds, and high-ionization lines (C IV) originate in the unbound outflowing gas (Collin-Souffrin et al. 1988).

For the γ-ray blazar 3C 454.3, León-Tavares et al. (2013) found a significant correlation between the increase in the Mg II flux density and the γ-ray flaring emission (in 2010 fall), which could be related to the superluminal radio component in this source. This implies that Mg II–emitting gas responds to the nonthermal continuum alongside the thermal continuum of the accretion disk. This is also in agreement with the significant correlation between the Mg II flux density and the γ-ray flux increase in the blazar CTA102 (Chavushyan et al. 2020), in which the superluminal radio component was also present. In addition, the Mg II broad line was broader and blueshifted at the maximum of the γ-ray activity in comparison to the minimum. The BLR material in this source was inferred to be located $\sim$25 pc from the central source. Chavushyan et al. (2020) conclude that the black hole mass estimation using Mg II is only reliable for the sources in which UV continuum is dominated by the central accretion disk, which is also the case for our source HE 0413, as we show in Section 6.3 based on the SED fitting, which is based on the thermal disk emission.

In summary, based on our findings and previous findings of other authors, a significant fraction of the Mg II–emitting gas is virialized and reverberating to the variable thermal continuum, as we also find in this work. For sources with a significant nonthermal emission due to the jet in the UV and the optical domain, outflowing gas at larger distances from the standard BLR region can respond to the nonthermal continuum, and this contributes to the broadening and a blueshifting of the Mg II line. Hence, when using the Mg II line in the reverberation studies, time-delay analysis should be complemented by SED modeling whenever possible to verify if photoionizing continuum is dominantly of thermal nature.

In terms of the quasar main sequence and the four-dimensional Eigenvector 1 (4DE1, Sulentic et al. 2000; Marziani et al. 2018), considering the equivalent width ($27.45^{+0.12}_{-0.10}$ Å) and the FWHM (4380^{+14}_{-15} km s^{-1}) exhibited by the Mg II line, HE 0413-4031 could be cataloged as a Population B1 in the 4DE1 scheme (Table 2 of Bachev et al. 2004). However, HE 0413-4031 shows a clear single-component Lorentzian profile associated with Population A sources (Section 2.3). According to the analysis presented

in Appendix C using a different model template for Fe II emission, the Mg II emission could also be modeled with two kinematic components, although their nature appears to be more problematic to interpret. Moreover, the FWHM of the 2 Gaussian components and their relative shift with respect to the Fe II emission depends strongly on the source redshift in the studied interval of $z \simeq 1.37$–1.39 (see our analysis in Appendix C, especially Figure C1).

As a high luminosity source, HE 0413-4031 can be found in the Population B spectral bins, being still a Population A source (Marziani et al. 2018). Because of its large Eddington ratio of $\sim$0.4, it can be further classified as an extreme Population A source (xA), with the Fe IIλ 4570 strength larger than unity $R_{\rm Fe\,II} > 1$, with the FWHM(Hβ) > 4000 km s^{-1} because the Mg II line is generally narrower than Hβ line. The difficult spectral-type classification of HE 0413-4031 stems from the fact that Population A sources are typically highly accreting sources with smaller black hole masses, and Population B sources have larger black hole masses and low Eddington ratios (Marconi et al. 2009; Fraix-Burnet et al. 2017). In this sense, HE 0413-4031 has mixed properties: a large black holes mass of a few $10^9 M_\odot$ and a high Eddington ration of $\sim$0.4. However, these general distinctions are based on the analyses of lower-luminosity low-redshift sources, while our source is at the intermediate redshift of $z \sim 1.4$ and of a high luminosity of 10^{47} erg s^{-1}. Hence the apparent discrepancy may be solved by the cosmological argumentation that the current massive black holes with low accretion rates were highly accreting sources at higher redshifts. With a black hole mass of a few billion solar masses, HE 0413 falls into the expected mass range for type 1 AGN between redshifts of 1 and 2 (see Figure 15 of Trakhtenbrot & Netzer 2012, where HE 0413 is located at the age of the universe of 4.66 Gyr for $z = 1.37$). On the other hand, HE 0413 is still an outlier in terms of the accretion rate close to the Eddington limit for a black hole mass of a few billion solar masses. Trakhtenbrot & Netzer (2012) suggest that a majority of such massive AGNs do not accrete close to their Eddington limits even at $z \simeq 2$.

Because HE 0413-4031 can be classified as a radio-loud AGN given its luminosity at 1.4 GHz, $L_{1.4} \approx 2.5 \times 10^{26}$ W Hz$^{-1} > 10^{24}$ W Hz^{-1} (Tadhunter 2016), its radio-optical properties can be studied in the broader context. Ganci et al. (2019) studied the radio properties of type-1 AGNs across all main spectral types along the quasar main sequence, in particular for three classes of Kellermann's radio-loudness criterion, which is defined as the ratio of the radio and optical flux densities, $R_{\rm K} = S_{\rm radio}/S_{\rm optical}$. We follow Ganci et al. (2019), who use 1.4 GHz flux density for $S_{\rm radio}$ and g-band flux density for $S_{\rm optical}$ and divide sources into three radio classes: radio detected (RD, $R_{\rm K} < 10$), radio intermediate (RI, $10 \leqslant R_{\rm K} < 70$), and radio-loud (RL, $R_{\rm K} \geqslant 70$). We derive the corresponding 1.4 GHz and g-band flux densities for HE 0413-4031 by linear interpolation of the averaged SED points in the log space (see Figure 9), $S_{1.4} = 21.04$ mJy and $S_g = 0.434$ mJy, which yields $R_{\rm K} = 48.5$. Hence, HE 0413-4031 can be classified as an RI source with an inverted and flat radio spectrum toward higher frequencies according to Vizier SED,[13] because the spectral index α, using the notation $S_\nu \propto \nu^{+\alpha}$, is $\alpha_{1-5} \simeq 0.7$, $\alpha_{5-8} \simeq 1.7$, $\alpha_{8-20} \simeq -0.02$ between 0.843 GHz, 5 GHz, 8 GHz, and 20 GHz, respectively. Sources with inverted to flat radio spectral indices are
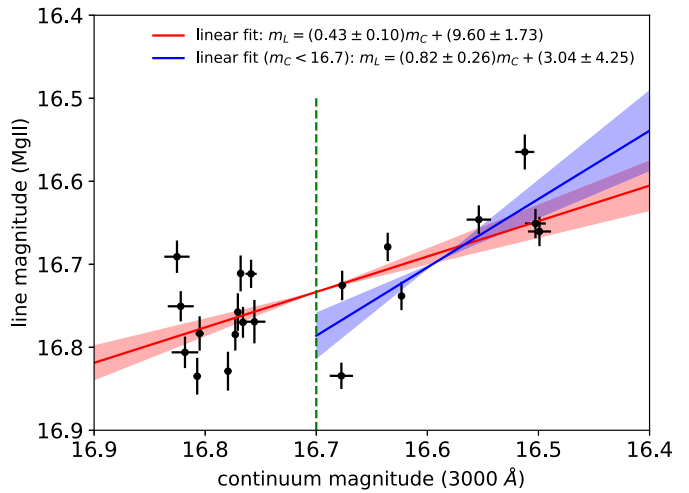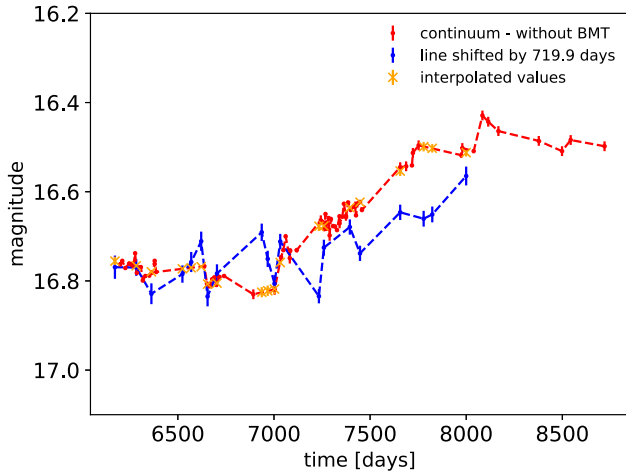
---

[13] http://vizier.u-strasbg.fr/vizier/sed

Figure 7. Determination of the continuum–line magnitude (luminosity) relation. Left panel: superposition of the continuum and the time-shifted line-emission lightcurves. Interpolated photometry points are also shown. Right panel: Mg II line-emission magnitude vs. continuum magnitude has a clear linear correlation in the logarithmic scale with the correlation coefficient of $r = 0.73$ ($R^2 = 0.53$), with the best-fit relation of $m_l = (0.43 \pm 0.10)m_c + (9.60 \pm 1.73)$. The blue line represents the linear fit to the data, with the continuum magnitude less than 16.7. In this case, the correlation coefficient is higher ($r = 0.79$, $R^2 = 0.63$) and the best-fit relation has a larger slope: $m_l = (0.82 \pm 0.26)m_c + (3.04 \pm 4.25)$.

characterized by a compact, optically thick radio core or a core-jet system (Zajaček et al. 2019a, 2019c).

Ganci et al. (2019) found that the occurrence of RD, RI, and RL sources differs along the main sequence. The classification of our source as RI with inverted-flat spectrum is consistent with its location in the extreme A population according to Ganci et al. (2019), because core-dominated sources in A3 and A4 bins are mostly RI. The source of radio emission in extreme A population can be partially due to a high star formation rate, but also the core-jet activity. In our case, the radio spectral index implies the presence of a compact core-jet system, hence the high star formation rate is not necessarily required. On the other hand, the presence of gas material is necessary to account for the high Eddington ratio of ~0.4–0.5. The optically thick radio core could be a sign of a restarted AGN activity (Czerny et al. 2009; Padovani et al. 2017), which will eventually heat up the cold gas content and/or blow it away and slow down the star formation.

6.2. Response of Mg II Emission to Continuum Changes— Intrinsic Baldwin Effect

The expected properties of the Mg II line were recently modeled by Guo et al. (2020), where the authors using the CLOUDY code and the locally optimally emitting cloud (LOC) scenario showed that at the high Eddington ratio of ~0.4, the Mg II line flux saturates and does not further increase with the rise of the continuum.

We confront this theoretical prediction with our observations of the quasar HE 0413-4031. We used the logarithm of both the continuum and Mg II line-emission flux densities, i.e., magnitudes. Subsequently, we applied the determined time-delay shift to the line emission, i.e., we shifted the Mg II lightcurve by 719.9 days in the observer's frame. For the continuum lightcurve, we tried both the cases with and without BMT data, by given the fact that the BMT data are present for the epochs longer than 8000 days, they do not have a significant effect on the following analysis. As the next step, we interpolate the photometry data to the time-shifted line-emission data to have corresponding line-continuum pairs. As before, given that the photometry data come from different instruments with various uncertainties, we make use of the weighted least-squares

linear B-spline interpolation with the inverse of uncertainties as weights. We show the continuum and the time-shifted line lightcurves in Figure 7 (left panel) alongside the interpolate values, which can also serve as a cross-check that the determined time-delay of ~720 days in the observer's frame represents the realistic similarity between the shapes of both lightcurves.

Finally, we plot the Mg II line magnitude with respect to the continuum magnitude in Figure 7 (right panel). This relation has a significant correlation with the correlation coefficient of $r = 0.73$. The best-fit linear relation is $m_l = (0.43 \pm 0.10)m_c + (9.60 \pm 1.73)$, which is displayed in Figure 7 with the corresponding uncertainties. Our linear fit implies directly the power-law relation between the Mg II and continuum luminosities, $L_{Mg\,II} \propto L_{3000}^{0.43 \pm 0.10}$. In combination with the measured time-delay of 303 days in the rest frame, we can conclude that the Mg II line responds to the continuum variability even for the source, which is highly accreting with the Eddington ratio of ~0.4 (see also Section 6.3 for a detailed SED modeling). Hence, our source does not exhibit a nonresponsive Mg II line with a rather constant dependency on the continuum luminosity, as was analyzed and shown by Guo et al. (2020) (see also their Figure 4). Moreover, from Figure 7 (right panel) it is apparent that the line and the continuum magnitudes consist of an uncorrelated part for continuum magnitudes of more than 16.7 mag (with the correlation coefficient of $r = 0.10$, $R^2 = 0.01$). The part of the dependency with continuum magnitudes less than 16.7 mag is strongly correlated with the correlation coefficient of $r = 0.79$ ($R^2 = 0.63$), and the best-fit linear fit is $m_l = (0.82 \pm 0.26)m_c + (3.04 \pm 4.25)$, hence the line luminosity responds even stronger to the continuum luminosity in this part with the relation $L_{Mg\,II} \propto L_{3000}^{0.82 \pm 0.26}$, which is marginally consistent with the linear dependency within the uncertainty.

Guo et al. (2020) analyze the LOC model and Mg II response for the smaller black hole mass and the 3000 Å luminosity ($M_\bullet = 10^8 M_\odot$ and $L_{3000} = 10^{44-45}$ erg s^{-1}). However, their upper limit for the Eddington ratio, $\eta_{Edd} = 0.4$, is comparable to our estimated Eddington ratio and hence their flattening of

Mg II luminosity close to $L_{3000} = 10^{45}$ erg s^{-1} is not confirmed for HE 0413-4031. On the other hand, we observe a similar dependency of the Mg II line luminosity on the continuum luminosity, as Guo et al. (2020) inferred for hydrogen recombination broad lines (Hα, Hβ) at lower Eddington ratios. For the luminosity range $\log[L_{3000}(\text{erg s}^{-1})] = 42$–44, the slope for H$\beta$ is $\alpha \sim 0.45$ and $\alpha \sim 0.42$ for Hα. In addition, Guo et al. (2020) show a slower rise of Mg II luminosity with respect to the continuum with the slope of $\sim$0.38, which is smaller than our value. This implies that at least for our source, the LOC model with the initial assumption of $(R_{\text{out}}, \Gamma) = (10^{17.5}, -2)^{14}$ does not apply.

The models with the larger radial extent of the BLR with $R_{\text{out}} = 10^{18}$ cm as shown in Figure 9 of Guo et al. (2020) seem to be more consistent with our slope of 0.43, as they show a continuous rise of Mg II luminosity even for larger continuum luminosities around the Eddington ratio of $\sim$0.4. This is also in agreement with our inferred travel distance of $R_{\text{Mg II}} = c\overline{\tau} = 0.254^{+0.020}_{0.016}$ pc $\sim 10^{17.9}$ cm. In comparison, the location of the dusty torus is still further. Its inner radius is given by the sublimation radius, $R_{\text{sub}} \sim 0.4$ pc $L_{45}^{0.5} T_{1500}^{-2.6} = 5.04$ pc $\sim 10^{19.2}$ cm (Elitzur & Shlosman 2006; Nenkova et al. 2008), for our estimate of the bolometric luminosity $L_{\text{bol}} = 1.589 \times 10^{47}$ erg s^{-1} and the dust sublimation temperature of 1500 K. The outer radius of the dusty torus is expected to be at $R_{\text{torus}} \sim Y R_{\text{sub}}$, where $Y \sim 5$–10 (Elitzur & Shlosman 2006). The light-travel distance, which can serve as a proxy for the BLR location in HE 0413-4031, is also in agreement with the model of the failed radiatively accelerated dusty outflow (FRADO, Czerny & Hryniewicz 2011). The failed dusty wind requires the existence of dust in the accretion disk, which is possible at and below $\sim$1000 K. This sets the inner radius of the BLR to $r_{1000}/R_{\text{sub}} = 0.03 M_8^{1/6}/(\dot{m}^{1/6}\eta_{0.1}^{1/2})$, where M_8 is the black hole mass scaled to $10^8 M_\odot$, $\dot{m} = \dot{M}/\dot{M}_{\text{Edd}}$ is the dimensionless accretion rate, and η is the accretion efficiency ($L_{\text{bol}} = \eta\dot{M}c^2$). Using the best-fit SED model, see Section 6.3, we adopt $M = 2.5 \times 10^9 M_\odot$, $\dot{m} = 0.51$, and $\eta = 0.1$, which leads to $r_{1000}/R_{\text{sub}} = 0.0574$ or $r_{1000} = 0.289$ pc $= 10^{17.95}$ cm, which is within uncertainties consistent with the light-travel distance $R_{\text{Mg II}}$. We illustrate these basic length-scales of the quasar HE 0413-4031 in Figure 8.

For the continuum magnitudes smaller than 16.7 mag, the slope of the line-continuum dependency (0.82 ± 0.26) is even larger than for the case when the whole range is considered. Interestingly, this slope is comparable to the exponent of the line-continuum relation as studied for the sample of flat-spectrum radio quasars (Patiño Álvarez et al. 2016), which is related to the global Baldwin effect between the equivalent width of originally broad UV lines (C IV, Lyα) and the corresponding continuum luminosities (at 1350 Å); see the original works by Baldwin (1977), Baldwin et al. (1978), and Wampler et al. (1984). In general, the equivalent width decreases with the increasing luminosity, which can be described as a power-law relation, $\text{EW}_{\text{line}} \propto L_{\text{cont}}^\gamma$. This can be rewritten as a relation between the line and the corresponding continuum luminosities using $\text{EW} \simeq L_{\text{line}}/L_{\text{cont}}$, which yields $L_{\text{line}} \propto L_{\text{cont}}^{\gamma+1}$. The original Baldwin effect is also called global or ensemble (Baldwin 1977; Carswell & Smith 1978), which is derived based on single-epoch observations of an
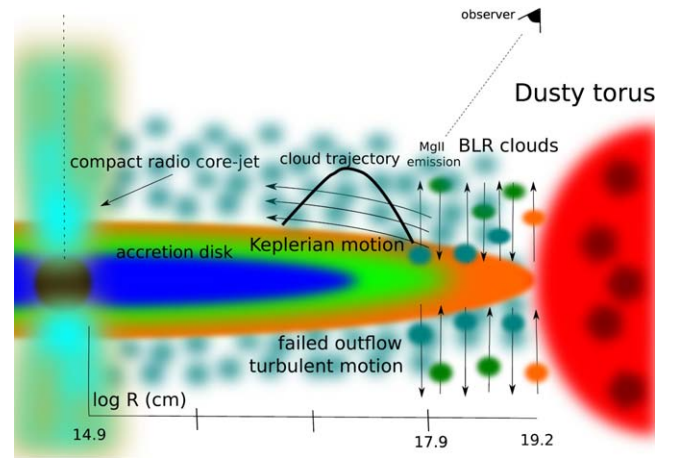

Figure 8. Illustration of the basic length-scales of the quasar HE 0413-4031. The BLR clouds are depicted with the dominantly Keplerian velocity field with a smaller outflow-inflow turbulent component according to the failed radiatively accelerated outflow model (FRADO, Czerny & Hryniewicz 2011). The axis along the bottom of the figure is expressed in the corresponding logarithms of basic radii in centimeters. From the left to the right side of the image, we include the Schwarzschild radius of $2.5 \times 10^9 M_\odot$ black hole, $\log R_{\text{Schw}} = 14.9$, the light-travel distance of Mg II emission, $\log R_{\text{Mg II}} = 17.9$, and the inner radius of the dusty torus, $\log R_{\text{sub}} = 19.2$.

ensemble of AGNs, while the analogical relation studied for individual AGNs is related to as an intrinsic Baldwin effect (Pogge & Peterson 1992).

Patiño Álvarez et al. (2016) analyze the line-continuum luminosity relation $L_{\text{line}}-L_{\text{cont}}$, including the Mg II line and 3000 Å continuum, for a sample of 96 FSRQ sources (core-jet blazars). For FSRQ, they found the slope of 0.796 ± 0.153, which is smaller than the slope of 0.909 ± 0.002 for the control sample of RQ AGN. Within uncertainties, their slope derived for the whole sample is comparable to our slope $L_{\text{Mg II}} \propto L_{3000}^{0.82\pm0.26}$. Hence, our detected intrinsic Baldwin effect is in agreement with the global one derived for the population of FSRQ. Previously, Rakić et al. (2017) studied the intrinsic Baldwin effect for 6 type-I AGN, and they detected it for the broad recombination lines, Hα and Hβ. They found that the intrinsic Baldwin effect is not related to the global one. Patiño Álvarez et al. (2016) found the difference of the global Baldwin effect between the radio-loud (blazar) and radio-quiet AGN, which could imply the importance of the nonthermal component, i.e., boosted jet emission, to the ionizing continuum for radio-loud sources. Apparently, more data for our quasar as well as more radio-loud and radio-quiet sources are needed to study in detail both the intrinsic and global Baldwin effect and their potential relation, especially taking into account the potential nonthermal contribution for radio-loud sources.

In summary, we detect a significant correlation between Mg II and the 3000 Å continuum after the removal of the light-travel time effect. The relation $L_{\text{line}}-L_{\text{cont}}$ is not linear, but has a slope of 0.43 ± 0.10 when all the corresponding line-luminosity points are combined. The slope is larger, $\gamma + 1 = 0.82 \pm 0.26$, when only a higher correlated part of the points is selected. These results are consistent with the Mg II broad-line emission being at least partially driven by the underlying continuum.

6.3. SED Fitting

Our determination of the black hole mass in Section 5.1 is not unique, because it requires additional assumptions about

---

[14] Locally optimally emitting cloud (LOC) models assume the power-law radial distribution of clouds, $f(r) \propto r^\Gamma$.
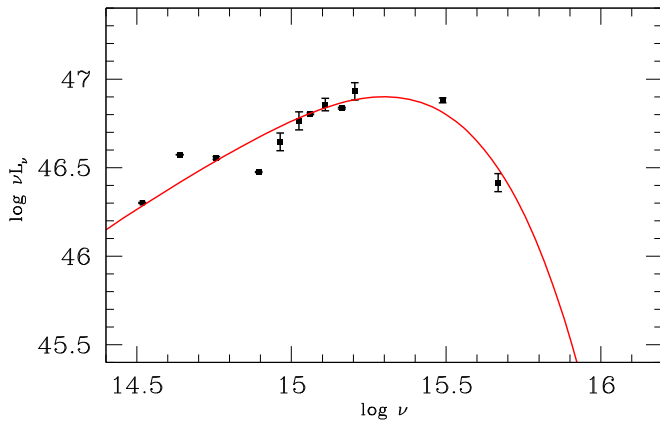
Figure 9. The SED data and the accretion disk model for HE 0413-4031 shown as the dependency of the luminosity νL_ν (in erg s^{-1}) on the frequency ν (in Hz) in the log space. The data are taken from the Vizier SED data (see http://vizier.u-strasbg.fr/vizier/sed). For the fitting, we use error-weighted averages of the data. The best-fit SED model is represented by a solid red line and is based on the parameters $M_\bullet = 3.0 \times 10^9 M_\odot$, $\dot{m} = 0.35$ (here measured in units of 1.678×10^{18} $(M/M_\odot$ g s^{-1})), $a = 0.31$, and $\iota = 34$ deg.

Table 3
Best-fitted Parameters for the Black Mass in the Range of $1–5 \times 10^9 M_\odot$

M ($10^9 M_\odot$)	Spin	$\dot{m}$	ι (deg)	χ^2
1	−0.99	1.81	0.0	31.57
1.5	−0.94	1.08	0.0	19.38
2	−0.13	0.60	0.0	19.54
2.5	0.025	0.51	33.8	19.17
3	0.46	0.31	25.8	19.31
3.5	0.52	0.26	33.6	19.23
4	0.44	0.29	49.8	20.20
4.5	0.0062	0.54	68.2	20.31
5	0.044	0.50	69.5	20.30

Note. The parameters include the spin, the accretion rate $\dot{m}$ (here measured in units of 1.678×10^{18} $(M/M_\odot$ g s^{-1})), and the viewing angle ι. The smallest χ^2 of 19.17 is for the case with the parameters $M = 2.5 \times 10^9 M_\odot$, $\dot{m} = 0.51$, $a = 0.025$, and $\iota = 33.8$ deg.

the virial factor. As a test of the mass range we obtained, we attempted to obtain the constraints for the black hole mass directly, from the accretion disk fitting to the continuum.

We used the data points available from Vizier SED photometric viewer.[15] After removal of the multiple entries and converting the measurements to the rest frame (assuming $z = 1.37648$ as determined in Section 3.1), and adopting $H_0 = 69.5$, $\Omega_m = 0.286$, $\Omega_L = 0.714$ (Bennett et al. 2014), we obtain the IR to UV SED (see Figure 9). We corrected the data for the Galactic extinction, although the effect is not strong in the direction of HE 0413-4031. The data points come from various epochs. Therefore, we added an additional error of 0.08 (in log space) to the measurements to account for the variability. For disk fitting, we used only points at the frequencies above 14.5 in the log scale, rest frame, because the rest frame near-IR emission in quasars comes from the hot dust component. We did not assume any presence of the blazar component because the data point did not seem to suggest its need.

We used the fully relativistic Novikov–Thorne model (Novikov & Thorne 1973), with all propagation effects as described in Czerny et al. (2011). The model is characterized by the black hole mass, accretion rate (in Eddington units, assuming the fixed efficiency of 1/12 in the definition, i.e., in units of 1.678×10^{18} $(M/M_\odot)$ g s^{-1}), spin, and viewing angle. We performed the fitting without constraints for any of those parameters. First, we performed the fitting for all the data points available, and we obtained the best-fit model with the parameters: $M = 3.0 \times 10^9 M_\odot$, $\dot{m} = 0.35$, $a = 0.31$, and $\iota = 34$ deg. We present this fit in Figure 9. Second, we also performed the fitting for the error-weighted averages of the data, and for the uncertainties we used error-weighted standard deviations. In this case, the best-fit solution was formally with the parameters: $M = 2.5 \times 10^9 M_\odot$, $\dot{m} = 0.51$, $a = 0.025$, and $\iota = 33.8$ deg. However, fits are highly degenerate, so the χ^2 allows for a broad mass range from $1 \times 10^9 M_\odot$ to masses even above $5 \times 10^9 M_\odot$ (see Table 3). Large masses, however, do not provide an acceptable solution because they also require a very high viewing angle. A high viewing angle is not expected because the unification scheme of AGN excludes it due to the

presence of the dusty/molecular torus (see, e.g., Padovani et al. 2017 for a recent review), and the clear excess in the near-IR shows that the torus is present in HE 0413-4031.

If we constrain the allowed parameters to $\iota < 45$ deg, the upper limit for the black hole mass is $M = 3.5 \times 10^9 M_\odot$. In our fits, the black hole spin is never large. For very small black hole masses, the accretion rate is super-Eddington and the spin is retrograde; the highest value of the spin we get is 0.52. However, this determination highly relies on one data point— the far-UV Galaxy Evolution Explorer measurement, which is in the spectral range where relativistic effects are important. If there is some internal reddening in the quasar, the allowed spin probably could be higher, but the SED data quality is not good enough to attempt more complex modeling.

The obtained black hole mass range $1.5 \times 10^9 M_\odot$–$3.5 \times 10^9 M_\odot$ is consistent with those presented in Section 5.1.

By integrating the best-fit SED, we can derive the bolometric correction BC for the monochromatic luminosity at 3000 Å. We obtain $L_{bol} = 2.8 L_{3000}$, which is smaller than the mean value of 5.62 ± 1.14 provided by Richards et al. (2006) for the same wavelength. However, it is consistent with the luminosity-dependent relation for the bolometric correction derived by Netzer (2019), which gives BC $= 25 \times (L_{3000}/10^{42}$ erg s$^{-1})^{-0.2} = 2.80$ for $L_{3000} = 10^{46.754}$ erg s^{-1}. The consistency with the power-law relation of Netzer (2019) stems from the fact that they used essentially the same model of an optically thick, geometrically thin accretion disk that is used in this work to fit the SED.

In summary, the SED fitting showed that the canonical thin, optically thick accretion disk can still account for the dominant part of the continuum in our highly accreting quasar. At higher accretion rates, the inner parts of the accretion flow are expected to become geometrically and optically thick, as in slim accretion disks, which can account for the reduction of the ionizing flux and shortening of time-delays (Wang et al. 2014b). This is indeed supported by the existence of stable geometrically thick and optically thick "puffy" accretion disks in global 3D GRMHD simulations for sub-Eddington accretion rates comparable to our values of $\dot{m} = 0.3$–0.6 (Lančová et al. 2019). However, the current computational facilities still do not allow a self-consistent treatment of the accretion disk-BLR dynamics on the scales of as much as 1000 gravitational radii, while the analytical and semi-analytical models explain the main observational features (Czerny et al. 2011; Czerny & Hryniewicz 2011).

---
[15] http://vizier.u-strasbg.fr/vizier/sed/

7. Conclusions

We summarize the main findings of the paper as follows:

1. Using seven different methods, we found a rest-frame time-delay between the continuum and Mg II line emission for the bright quasar HE 0413-4031, $\overline{\tau} = 302.6^{+28.7}_{-33.1}$ days, which was the most frequent peak in time-delay distributions.

2. In combination with the data for 10 other sources monitored in the Mg II line, we construct a radius–luminosity relation, which is consistent with the theoretically expected dependency, $R \propto L^{1/2}$. The new quasar HE 0413-4031 with the monochromatic luminosity of $\log L_{3000} = 46.754^{+0.028}_{-0.132}$ lies below the expected relation, which can be explained by its higher accretion rate. In general, for all Mg II sources, the departure from the radius–luminosity relation, i.e., the shortening of their time-delays, is larger for higher-accreting sources. The same effect was previously observed for the sources monitored in $H\beta$.

3. We determined the response of the Mg II line luminosity to the photoionizing continuum luminosity, $L_{\rm line} \propto L_{\rm cont}^{0.43 \pm 0.10}$, which is comparable to the response of recombination emission lines $H\alpha$ and $H\beta$, according to theoretical photoionization models. This is consistent with the outer radius of the BLR at $R_{\rm out} = 10^{18}$ cm, which is in turn in agreement with the light-travel distance inferred from the rest-frame time-delay.

4. The virial black hole mass determined based on the measured rest-frame time-delay, $M_{\rm RM}^{\rm uncorr}(f = 1) \simeq 1.1 \times 10^9\,M_\odot$, is smaller by a factor of 4 than the value expected from the radius–luminosity relation, $M_{\rm RM}^{\rm corr}(f = 1) \simeq 4.6 \times 10^9\,M_\odot$.

The black hole mass inferred from fitting a thin accretion disk model to the source SED, $M_{\rm SED} = 1.5 \times 10^9 M_\odot$–$3.5 \times 10^9 M_\odot$, is in agreement with these values within the uncertainty. Other best-fitted parameters for the source are the Eddington ratio of $0.26 \leqslant \dot{m} \leqslant 1.08$, the black hole spin of $-0.94 \leqslant a \leqslant 0.52$, and the viewing angle of $0 \leqslant \iota \leqslant 34$ degrees.

Appendix A
Photometric and Spectroscopic Data

In this section, we summarize the characteristics of Fe II and Mg II lines in Table A1, where we specifically list the Fe II and

Table A1
Table of Fe II and Mg II Equivalent Widths in Å, Velocity Shift in km s^{-1}, Line Width in Å, and the Mg II Flux Density in erg s^{-1} cm^{-2} Å^{-1}

Obs. No.	JD $-2\,450\,000$	EW(Fe II) Å	EW(Mg II) Å	Shift km s^{-1}	Width Å	Flux density erg s^{-1} cm^{-2} Å^{-1}
1	6314.4087	$13.71^{+0.91}_{-0.93}$	$34.18^{+0.51}_{-0.49}$	$1666.98^{+17.04}_{-16.65}$	$2149.29^{+28.50}_{-40.08}$	$(3.836 \pm 0.074) \times 10^{-14}$
2	6320.3859	$9.75^{+1.34}_{-1.32}$	$35.89^{+0.79}_{-0.74}$	$1723.70^{+23.73}_{-22.96}$	$2196.68^{+54.72}_{-52.86}$	$(4.000 \pm 0.114) \times 10^{-14}$
3	6523.5954	$10.73^{+2.28}_{-2.22}$	$34.67^{+1.25}_{-1.20}$	$1529.11^{+39.28}_{-39.12}$	$2165.96^{+88.44}_{-81.07}$	$(3.966 \pm 0.178) \times 10^{-14}$
4	6651.4751	$10.38^{+1.77}_{-1.72}$	$36.59^{+1.04}_{-1.02}$	$1598.83^{+31.86}_{-31.09}$	$2289.73^{+81.43}_{-64.80}$	$(4.051 \pm 0.152) \times 10^{-14}$
5	6697.3600	$14.13^{+1.32}_{-1.34}$	$37.93^{+0.78}_{-0.75}$	$1617.81^{+22.58}_{-22.60}$	$2316.05^{+46.37}_{-61.37}$	$(4.219 \pm 0.114) \times 10^{-14}$
6	6892.5678	$17.07^{+1.11}_{-1.03}$	$36.06^{+0.56}_{-0.58}$	$1554.76^{+18.02}_{-18.05}$	$2218.54^{+41.03}_{-38.86}$	$(3.911 \pm 0.094) \times 10^{-14}$
7	7003.5182	$13.25^{+0.58}_{-0.64}$	$35.64^{+0.36}_{-0.34}$	$1608.01^{+11.37}_{-11.35}$	$2307.95^{+24.90}_{-23.98}$	$(3.908 \pm 0.067) \times 10^{-14}$
8	7082.2985	$13.29^{+0.83}_{-0.82}$	$31.20^{+0.48}_{-0.44}$	$1615.91^{+17.11}_{-17.14}$	$2300.84^{+46.54}_{-35.14}$	$(3.702 \pm 0.080) \times 10^{-14}$
9	7243.6124	$13.93^{+0.69}_{-0.72}$	$30.65^{+0.41}_{-0.36}$	$1597.95^{+14.64}_{-14.64}$	$2250.33^{+34.74}_{-28.81}$	$(3.856 \pm 0.069) \times 10^{-14}$
10	7289.4741	$13.57^{+0.89}_{-0.86}$	$31.14^{+0.47}_{-0.46}$	$1613.10^{+17.51}_{-17.45}$	$2213.75^{+45.45}_{-31.14}$	$(3.953 \pm 0.082) \times 10^{-14}$
11	7341.3298	$12.46^{+0.82}_{-0.87}$	$32.33^{+0.45}_{-0.49}$	$1597.92^{+16.98}_{-17.10}$	$2296.71^{+40.25}_{-39.59}$	$(4.127 \pm 0.082) \times 10^{-14}$
12	7374.4950	$13.43^{+0.83}_{-0.83}$	$28.87^{+0.43}_{-0.45}$	$1594.19^{+19.07}_{-17.77}$	$2200.05^{+36.00}_{-35.27}$	$(3.681 \pm 0.075) \times 10^{-14}$
13	7423.3702	$10.12^{+0.74}_{-0.72}$	$29.97^{+0.41}_{-0.44}$	$1669.13^{+16.79}_{-16.53}$	$2331.95^{+34.35}_{-39.93}$	$(3.860 \pm 0.073) \times 10^{-14}$
14	7656.2474	$10.64^{+0.63}_{-0.61}$	$28.06^{+0.36}_{-0.33}$	$1664.97^{+14.98}_{-13.65}$	$2290.71^{+35.96}_{-30.11}$	$(4.204 \pm 0.075) \times 10^{-14}$
15	7687.3943	$10.65^{+0.65}_{-0.62}$	$28.08^{+0.36}_{-0.35}$	$1664.77^{+15.31}_{-14.89}$	$2288.94^{+37.67}_{-30.63}$	$(3.979 \pm 0.067) \times 10^{-14}$
16	7722.5591	$11.99^{+0.66}_{-0.66}$	$26.62^{+0.38}_{-0.34}$	$1672.60^{+16.16}_{-15.95}$	$2254.84^{+29.84}_{-40.84}$	$(3.781 \pm 0.066) \times 10^{-14}$
17	7752.4673	$10.26^{+0.58}_{-0.58}$	$27.94^{+0.34}_{-0.32}$	$1682.02^{+14.26}_{-14.03}$	$2298.09^{+29.95}_{-33.91}$	$(4.125 \pm 0.065) \times 10^{-14}$
18	7953.6598	$12.10^{+0.64}_{-0.64}$	$25.37^{+0.33}_{-0.34}$	$1648.26^{+15.85}_{-15.69}$	$2208.36^{+32.31}_{-31.79}$	$(3.683 \pm 0.054) \times 10^{-14}$
19	7979.5920	$11.83^{+0.59}_{-0.62}$	$28.05^{+0.35}_{-0.35}$	$1640.45^{+14.78}_{-14.73}$	$2363.17^{+33.85}_{-35.90}$	$(4.072 \pm 0.067) \times 10^{-14}$
20	8114.4800	$10.35^{+0.56}_{-0.65}$	$27.40^{+0.36}_{-0.32}$	$1681.22^{+14.14}_{-14.81}$	$2337.25^{+33.20}_{-37.38}$	$(4.250 \pm 0.067) \times 10^{-14}$
21	8167.3265	$9.26^{+0.53}_{-0.58}$	$26.59^{+0.34}_{-0.27}$	$1649.54^{+14.75}_{-14.32}$	$2358.10^{+33.34}_{-34.15}$	$(4.025 \pm 0.063) \times 10^{-14}$
22	8376.5021	$13.63^{+0.65}_{-0.62}$	$29.30^{+0.36}_{-0.35}$	$1631.38^{+14.73}_{-14.41}$	$2326.37^{+30.10}_{-29.91}$	$(4.380 \pm 0.069) \times 10^{-14}$
23	8498.4167	$10.98^{+0.61}_{-0.65}$	$29.25^{+0.37}_{-0.37}$	$1800.13^{+15.32}_{-14.75}$	$2343.83^{+30.65}_{-41.66}$	$(4.323 \pm 0.070) \pm 10^{-14}$
24	8543.3100	$8.85^{+0.61}_{-0.62}$	$29.55^{+0.38}_{-0.36}$	$1751.82^{+15.48}_{-14.00}$	$2368.61^{+33.36}_{-42.12}$	$(4.361 \pm 0.071) \times 10^{-14}$
25	8719.5708	$15.47^{+0.94}_{-0.91}$	$32.19^{+0.54}_{-0.52}$	$1667.05^{+19.55}_{-19.16}$	$2359.25^{+52.31}_{-40.14}$	$(4.722 \pm 0.092) \times 10^{-14}$

Note. The flux density was calculated for the case without the BMT data; see the text for the description.

Table A2
Table of Continuum Magnitudes with Uncertainties

JD −2450,000	Magnitude (V band) mag	Error mag	Instrument No.
6199.79634	16.763	0.005	1
6210.81464	16.755	0.003	1
6226.67656	16.771	0.004	1
6246.69516	16.761	0.004	1
6257.74660	16.763	0.005	1
6268.68051	16.767	0.004	1
6277.68239	16.738	0.003	1
6286.66584	16.782	0.004	1
6297.61482	16.770	0.004	1
6307.57245	16.769	0.004	1
6317.63928	16.799	0.004	1
6330.65489	16.789	0.003	1
6351.54598	16.788	0.004	1
6363.57130	16.782	0.003	1
6379.48424	16.762	0.004	1
6379.49181	16.755	0.004	1
6387.50984	16.780	0.003	1
6637.66923	16.767	0.003	1
6651.62009	16.806	0.003	1
6665.60325	16.812	0.004	1
6678.59717	16.796	0.003	1
6689.67132	16.792	0.003	1
6700.63473	16.809	0.004	1
6715.57393	16.791	0.003	1
6740.48864	16.789	0.004	1
6892.59242	16.830	0.011	2
7003.54330	16.819	0.012	2
7036.65108	16.747	0.004	1
7048.65280	16.731	0.003	1
7060.60356	16.700	0.004	1
7082.30016	16.749	0.012	2
7084.53369	16.732	0.005	1
7118.50567	16.731	0.005	1
7243.61293	16.664	0.011	2
7253.88913	16.668	0.003	1
7261.88037	16.684	0.004	1
7267.91217	16.650	0.004	1
7273.84457	16.683	0.004	1
7283.84655	16.659	0.004	1
7289.47056	16.698	0.012	2
7295.84011	16.661	0.004	1
7306.77839	16.677	0.004	1

Note. The epoch is given in Julian dates (−2450,000). The last column denotes three different instruments used to obtain the photometry data: 1. OGLE, 2. SALTICAM, 3. BMT. The BMT photometry points were shifted by 0.171 mag to larger magnitudes to match the last OGLE point with the closest BMT point in the lightcurve.

Table A3
Table of Continuum Magnitudes with Uncertainties

JD −2450,000	Magnitude (V band) mag	Error mag	Instrument No.
7317.73770	16.678	0.004	1
7327.77204	16.686	0.004	1
7340.70393	16.655	0.003	1
7341.32488	16.671	0.011	2
7355.69184	16.656	0.004	1
7363.66368	16.627	0.003	1
7374.49091	16.654	0.011	2
7374.70619	16.657	0.003	1

Table A3
(Continued)

JD −2450,000	Magnitude (V band) mag	Error mag	Instrument No.
7385.55446	16.624	0.003	1
7398.61439	16.641	0.003	1
7415.58224	16.634	0.003	1
7423.36782	16.633	0.011	2
7426.56315	16.653	0.003	1
7436.52206	16.626	0.004	1
7447.52422	16.623	0.003	1
7457.51899	16.641	0.003	1
7656.47709	16.545	0.011	2
7687.38749	16.543	0.011	2
7717.70291	16.541	0.003	1
7722.55378	16.513	0.011	2
7752.46369	16.496	0.011	2
7973.91046	16.518	0.006	1
7979.59391	16.502	0.011	2
8038.85902	16.509	0.004	1
8084.30756	16.429	0.011	2
8090.70000	16.338	0.008	3
8114.47660	16.193	0.011	2
8138.70000	16.305	0.008	3
8139.60000	16.311	0.004	3
8146.60000	16.284	0.003	3
8165.60000	16.296	0.005	3
8167.32241	16.464	0.011	2
8173.60000	16.277	0.007	3
8180.50000	16.261	0.006	3
8196.50000	16.291	0.008	3
8205.50000	16.274	0.006	3
8365.90000	16.285	0.006	3
8377.50208	16.486	0.011	2
8386.90000	16.302	0.008	3
8414.80000	16.319	0.005	3
8498.41249	16.509	0.011	2
8543.30431	16.484	0.011	2
8566.50000	16.319	0.008	3
8719.57089	16.498	0.011	2

Note. The epoch is given in Julian dates (−2450 000). The last column denotes three different instruments used to obtain the photometry data: 1. OGLE, 2. SALTICAM, 3. BMT. The BMT photometry points were shifted by 0.171 mag to larger magnitudes to match the last OGLE point with the closest BMT point in the lightcurve.

Mg II equivalent widths in Å, velocity shift in $km\,s^{-1}$, line width in Å, and the Mg II flux density in $erg\,s^{-1}\,cm^{-2}\,\mathring{A}^{-1}$. The continuum magnitudes (V band) from the three instruments—OGLE, SALTICAM, and BMT—are included in Tables A2 and A3.

Appendix B
Overview of Time-delay Determination Methods

B.1. Interpolated Cross-correlation Function (ICCF)

The ICCF is a standard method for determining the time-delay between the continuum and line-emission lightcurves. In general, both lightcurves are unevenly sampled, while the ICCF by its definition requires regular sampling with a certain time-step, which is achieved by the interpolation of the continuum lightcurve with respect to the line-emission lightcurve or vice versa (asymmetric ICCF). The definition of the ICCF
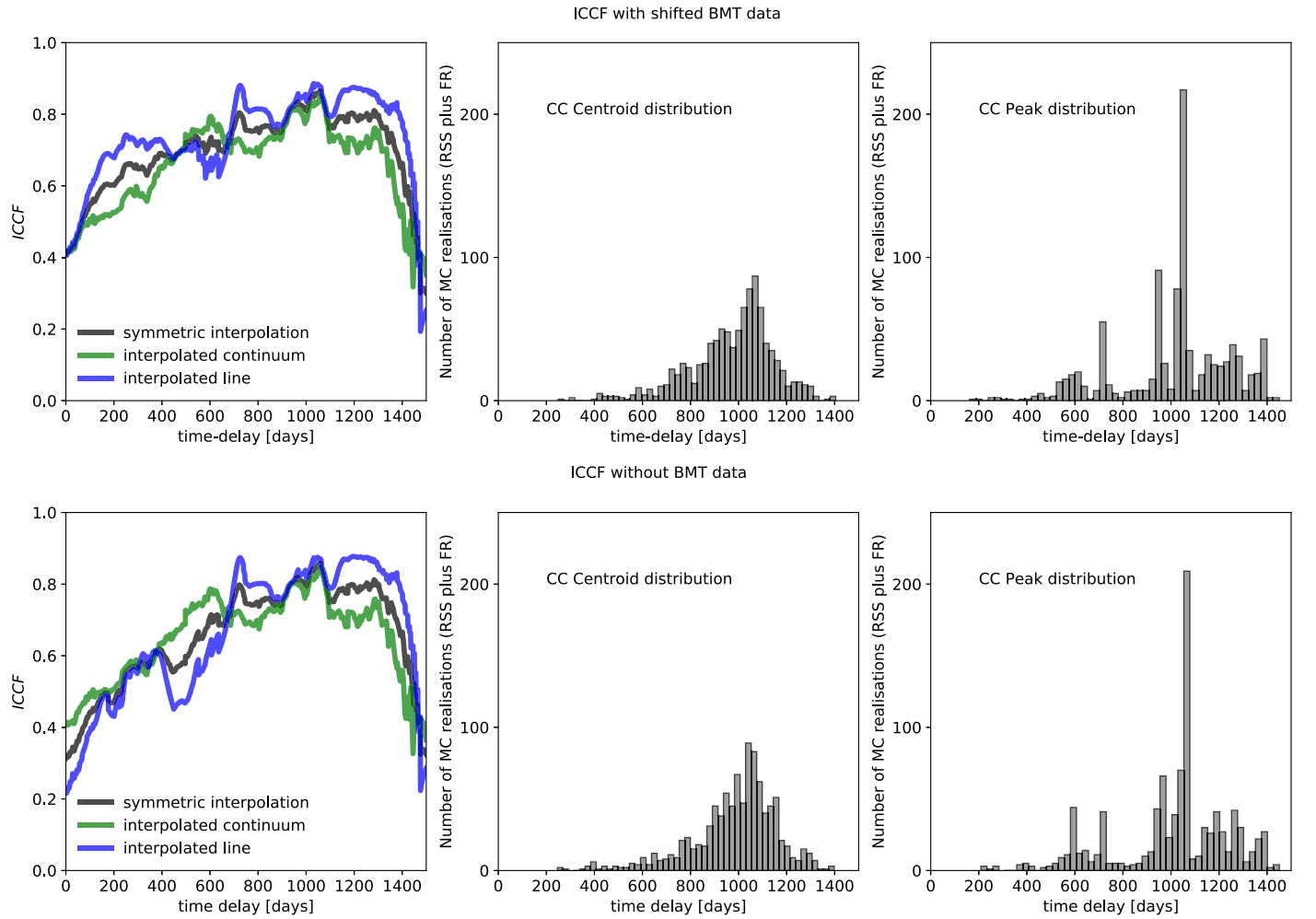
Figure B1. Interpolated cross-correlation coefficient as a function of time-delay in the observer's frame. Top panel: the interpolated cross-correlation function (ICCF) as a function of time-delay, including shifted BMT points. The middle panel displays the distribution of cross-correlation centroids, while the right panel shows the distribution of cross-correlation peaks. Bottom panel: the same as in the top panel but without BMT data.

between the two lightcurves, x_i and y_i, with the step-size of $\Delta t = t_{i+1} - t_i$, is

$$CCF(\tau_k) = \frac{\left(1/N\right)\sum_{i=1}^{N-k}(x_i - \bar{x})(y_{i+k} - \bar{y})}{\left[(1/N)\sum_i^N(x_i - \bar{x})^2\right]^{1/2}\left[(1/N)\sum_i^N(y_i - \bar{y})^2\right]^{1/2}}, \quad \text{(B1)}$$

where τ_k is the time-shift $\tau_k = k\Delta t$, where the index $k = 1, ..., N - 1$, of the second lightcurve with respect to the first one, and where $\bar{x}$ and $\bar{y}$ are the means of the two lightcurves x_i and y_i. The final, symmetric ICCF is obtained by averaging the ICCFs from both interpolations.

We apply the Python implementation of ICCF, the script PYCCF (Sun et al. 2018) based on an earlier ICCF analysis of Peterson et al. (1998), which calculates the ICCF including the continuum, line-emission, and symmetric interpolation. Using 1,000 Monte Carlo realizations of random subset selection (RSS) and flux randomization (FR), we obtained ICCF peak and centroid distributions, including their corresponding uncertainties.

First, we cross-correlated the full continuum lightcurve, which included SALTICAM, OGLE, and flux-shifted BMT data, in total 86 points, with the Mg II lightcurve (25 points). In

addition, given the systematic offset of the BMT flux densities from SALTICAM points, we decided to perform the ICCF analysis also without them, which reduced the photometric lightcurve to 73 points. The ICCF values with respect to the time-delay, for which we separately calculated the continuum-interpolated, line-interpolated, and symmetric ICCF, with the corresponding peak and centroid distributions (for symmetric CCF) are displayed in Figure B1 with and without BMT points in the top and bottom panels, respectively. We summarize the peak and centroid values of the ICCF for the interpolated continuum, interpolated line-emission, and symmetric case in Table B1, where the cases with and without BMT data points are separated as well. When comparing these two cases in Table B1, the peak and centroid values for the case without the BMT data are generally comparable within the uncertainties, which is also visible in centroid and peak distributions in Figure B1.

The maximum values of the ICCF are about 0.8 (for the interpolation of the photometry), which for such a relatively short emission-line lightcurve is a high value, supporting the view that the delay determination should be in general reliable because the line and continuum are well correlated. For comparison, the maximum value of the ICCF for the quasar CTS C30.10, with similar formal data quality, was only 0.65 (Czerny et al. 2019; Zaja¢ek et al. 2019b).

Table B1
Results of the Interpolated Cross-correlation Function Applied to HE 0413-84031 Lightcurves

	With Shifted BMT Data	Without BMT Data
Interpolated continuum—centroid [days]	$1004.6^{+196.8}_{-246.2}$	$1003.2^{+205.3}_{-235.4}$
Interpolated continuum—peak [days]	$1060.0^{+228.0}_{-342.6}$	$1061.0^{+228.2}_{-270.8}$
Interpolated line—centroid [days]	$1008.4^{+142.2}_{-276.9}$	$1034.171^{+139.1}_{-248.9}$
Interpolated line—peak [days]	$984.0^{+227.6}_{-349.0}$	$1001.0^{+252.3}_{-282.0}$
Symmetric—centroid [days]	$1009.7^{+113.6}_{-211.5}$	$1021.7^{+114.5}_{-207.8}$
Symmetric—peak [days]	$1056.0^{+197.0}_{-332.1}$	$1057.0^{+196.0}_{-343.8}$

Note. We include centroids and peaks with uncertainties for interpolated continuum lightcurve, interpolated emission lightcurve, and symmetric ICCF. Cases with and without BMT data are separated. The time-delays are expressed in light days in the observer's frame.

Table B2
Time-delay in Light Days Corresponding to the Peak Values of DCF in the Observer's Frame

	With Shifted BMT Data	Without BMT Data
Time-delay at the DCF peak (0,1500; 120)	812.7 (DCF = 0.82)	812.7 (DCF = 0.80)[1]
Time-delay at the DCF peak (200,1100; 20)	730.0 (DCF = 0.93)	730.0 (DCF = 0.92)
Peak time-delay—bootstrap [days]	$720.4^{+115.1}_{-147.9}$	$726.0^{+114.4}_{-145.7}$
Mean time-delay—bootstrap [days]	$658.7^{+116.2}_{-139.2}$	$665.4^{+115.0}_{-142.8}$

Note. Two time intervals are analyzed: between 0 and 1500 days, and the narrower interval between 200 and 1100 days. The bottom two lines show the peak and the mean time-delay as inferred from 500 bootstrap realizations. (1) This is the value for the maximum DCF for time-delays less than 1300 days; the time-delay at 1315 days has the larger DCF of 0.82, but this value can be excluded as it approaches the end of the observational run.

We also tested if the linear trend present in the continuum should be eventually subtracted before the time-delay is measured. However, we noticed that such a trend subtraction decreases the maximum value of the correlation in ICCF. For example, for the interpolated continuum, without BMT data points, r_{max} decreases from 0.85 down to 0.61. Thus we conclude that the trend subtraction is not beneficial for the time-delay analysis. The presence of the trend is natural if the lightcurve of the red noise character, as here, covers the period shorter than the maximum timescale present in the system. The time-delay measurement is not strongly affected anyway; we obtain for the same case the peak time-delay of 1037.0 days instead of 1061.0 days. Thus, in further analysis, we do not consider the trend subtraction.

B.2. Discrete Correlation Function (DCF)

Edelson & Krolik (1988) suggested using the DCF because the ICCF by definition introduces additional interpolated data points and can thus distort the time-delay determination, especially for the unevenly and sparsely sampled pairs of lightcurves. The basic algorithm is to search for data pairs (x_i, y_j) between the two lightcurves that fall into the time-delay bin $\tau - \delta\tau/2 \leqslant \Delta t_{ij} < \tau + \delta\tau/2$, where τ is the time-delay, $\delta\tau$ is the chosen time-delay bin, and $\Delta t_{ij} = t_j - t_i$. Given M such pairs, we can calculate the unbinned discrete correlation coefficient for each of them,

$$\text{UDCF}_{ij} = \frac{(x_i - \bar{x})(y_j - \bar{y})}{\sqrt{(s_x - \sigma_x^2)}\sqrt{(s_y - \sigma_y^2)}}, \qquad (B2)$$

where $\bar{x}$ and $\bar{y}$ are the lightcurve means in the given time-delay bin; s_x, s_y are the variances; and σ_x, σ_y are the mean measurement errors for a given bin. The discrete correlation function for a given time-delay is calculated by averaging over

M data point pairs,

$$\text{DCF}(\tau) = \frac{1}{M}\sum_{ij}\text{UDCF}_{ij}. \qquad (B3)$$

The error of the DCF can be formally inferred from the relation

$$\sigma_{\text{DCF}}(\tau) = \frac{1}{M-1}\sqrt{\sum[\text{UDCF}_{ij} - DCF(\tau)]^2}. \qquad (B4)$$

For our DCF analysis, we make use of the Python code pyDCF by Robertson et al. (2015) with the possibility of applying the Gaussian weighting scheme to matching pairs of both lightcurves. We also tested different time-delay bins as well as the searched time-delay intervals. In addition, we extended the DCF analysis by including the bootstrap technique to construct time-delay distributions and to infer the actual peaks and their uncertainties.

We explore the correlation of the two lightcurves on two timescales:

1. Between 0 and 1500 days, with a time-step of 120 days,
2. Between 200 and 1100 days, with a smaller time-step of 20 days.

As before for the ICCF analysis, we perform the DCF analysis with and without flux-shifted BMT data. The time-delays for the peak values of the DCF are shown in Table B2. The figures of the DCF versus the time-delay are in Figure B2 for the case with and without BMT data points in the left and right panels, respectively. In the top panels of Figure B2, we show the whole explored time-range between 0 and 1500 days (with a time-step of 120 days); in the bottom panels, we display the DCF analysis in the time-range (200, 1100) days with a smaller time-step of 20 days.

To determine the uncertainty of the DCF peaks as well as the mean values for the time-delay, we perform 500 bootstrap simulations by randomly selecting subsamples of the
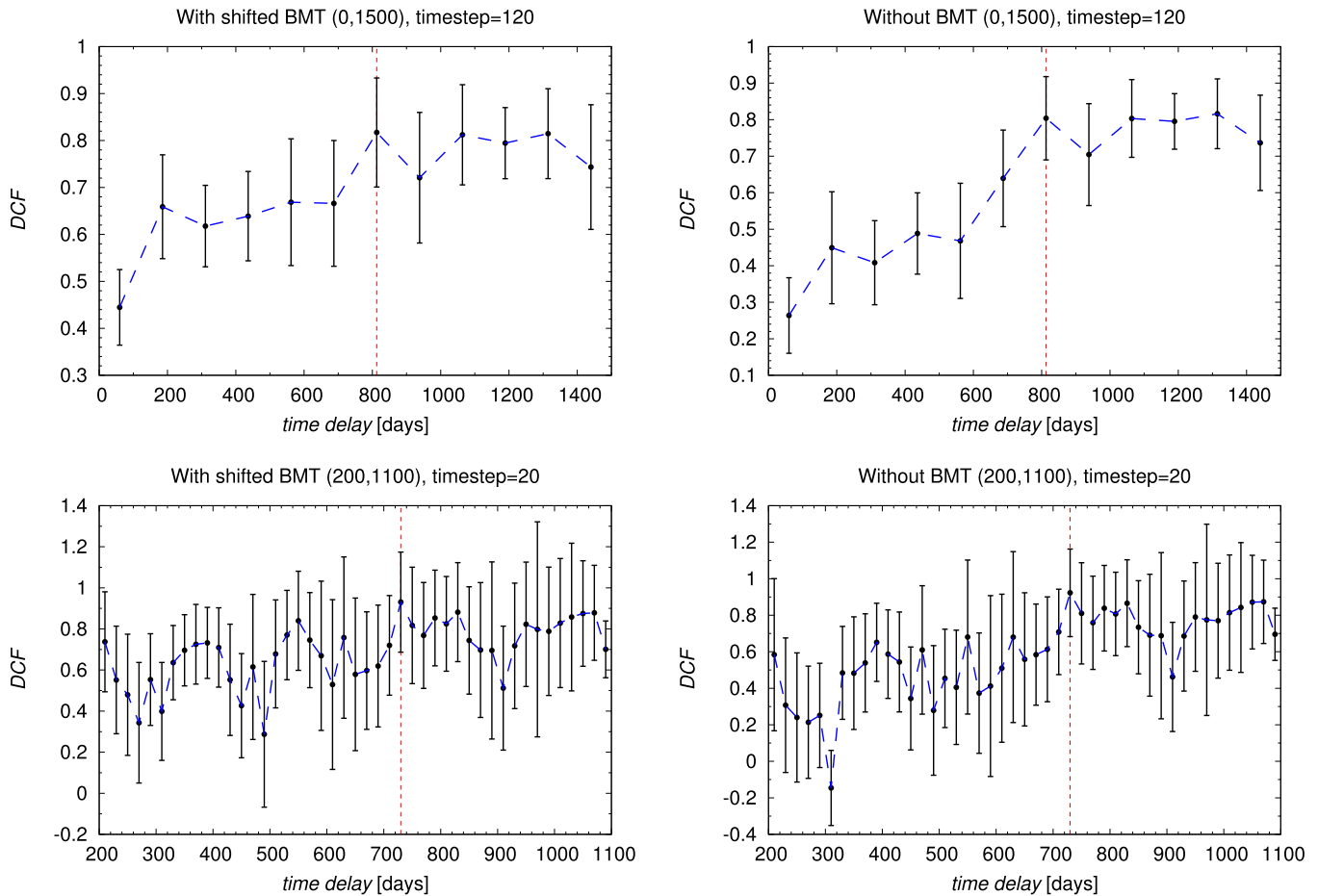
Figure B2. The discrete correlation function (DCF) as a function of the time-delay in the observer's frame. Top panels: the DCF determined between 0 and 1500 days, with a time-step of 120 days. To the left we include the shifted BMT flux densities for the continuum; to the right, they are omitted. The vertical dashed line denotes the time-delay for the maximum DCF. Bottom panels: similar to the panel above, the DCF analysis was performed for the time-interval of 200–1100 days with a smaller time-step of 20 days. The vertical dashed line denotes the time-delay for the maximum DCF.

lightcurves for both the cases with the flux-shifted BMT data and without them. The values of the peak and mean time-delays are in Table B2. The peak time-delay (for the largest DCF value) is clearly in the interval around 720–730 days, as is also visible in the histograms in Figure B3 for both the cases with and without BMT data in the left and right panels, respectively.

B.3. z-transformed Discrete Correlation Function (zDCF)

Alexander (1997) proposed the zDCF to correct several biases of the classical DCF (Edelson & Krolik 1988); namely, it replaces equal time-lag binning with equal population binning and uses Fisher's z-transform. The minimum required number of observed points is 11; therefore, the z-transformed DCF is specially suited for undersampled, sparse and heterogeneous pairs of lightcurves, which is the case for our continuum and line-emission lightcurves, as they are combined from different instruments. In addition, zDCF does not assume any lightcurve properties, such as smoothness, or any AGN variability process. Moreover, from Monte Carlo generated pairs of lightcurves with randomized errors, it is possible to infer the uncertainty from the averaged zDCF values.

For our zDCF analysis, we first used 86 continuum measurements (including data from OGLE, SALTICAM, and flux-corrected BMT) and 25 Mg II line-emission points (from SALT spectral observations). The zDCF values as a function of

the time-delay are displayed in Figure B4, including both errors for the time-delay and the zDCF value. Two peaks are apparent, $\tau_1 = 720.9$ days with $z\mathrm{DCF} = 0.92$, and $\tau_2 = 1059$ days with $z\mathrm{DCF} = 0.91$. To evaluate the uncertainties of these peaks, we ran the maximum-likelihood (ML) analysis for the surroundings of each peak, between 500 and 1000 days for the peak at 721 days and 1000 and 1500 days for the peak at 1059 days. In the next step, we performed global ML analysis of the time-delay peaks between 0 and 2000 days, with the most likely peak at 721^{+324}_{-527} days. The results are shown in Table B3 (left column).

In the continuum lightcurve, the BMT points needed to be systematically shifted toward smaller flux densities to match OGLE and SALTICAM values. Therefore we also performed zDCF analysis without BMT points, with the total of 73 continuum points and 25 Mg II line-emission points. The overall results concerning the time-delay peaks were not affected; see Table B3 (right column) and Figure B4 (right panel). The global peak remained at $720.9^{+331.3}_{-100.1}$ days with a smaller lower uncertainty interval than for the case including BMT data points, but with a comparable likelihood value.

B.4. The JAVELIN Code Package

Another way of estimating the time-delay is to model the AGN continuum variability as a stochastic process via the
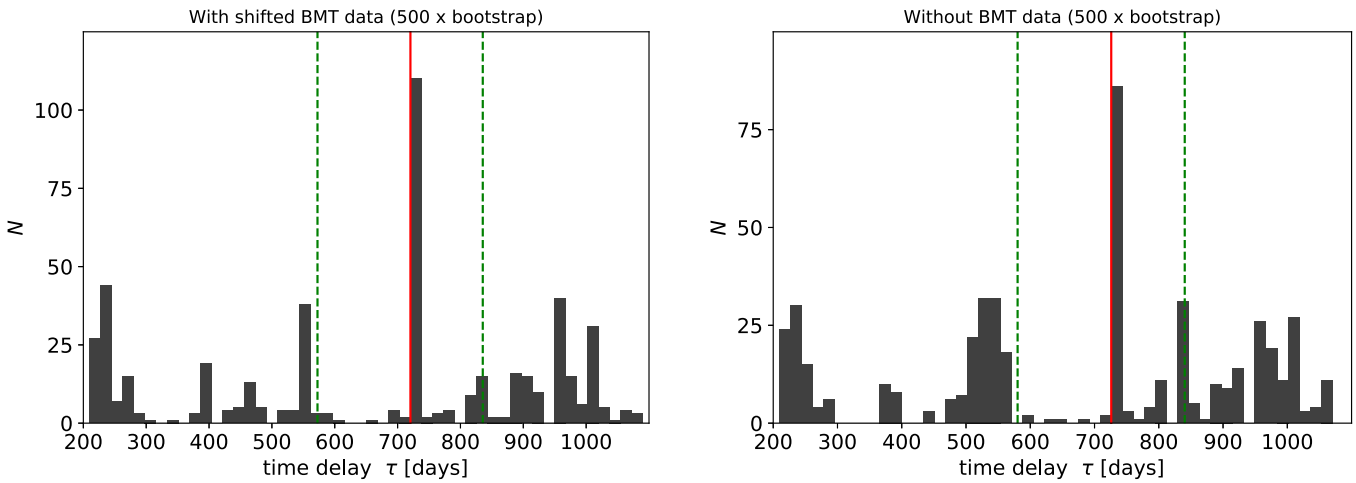
Figure B3. Histograms of the time-delays constructed from 500 bootstrap realizations of the DCF analysis. Left panel: with flux-shifted BMT data included. Right figure: without BMT data. In both panels, the red vertical line marks the histogram peak value, and the two green horizontal lines stand for 1σ uncertainties of the peak.
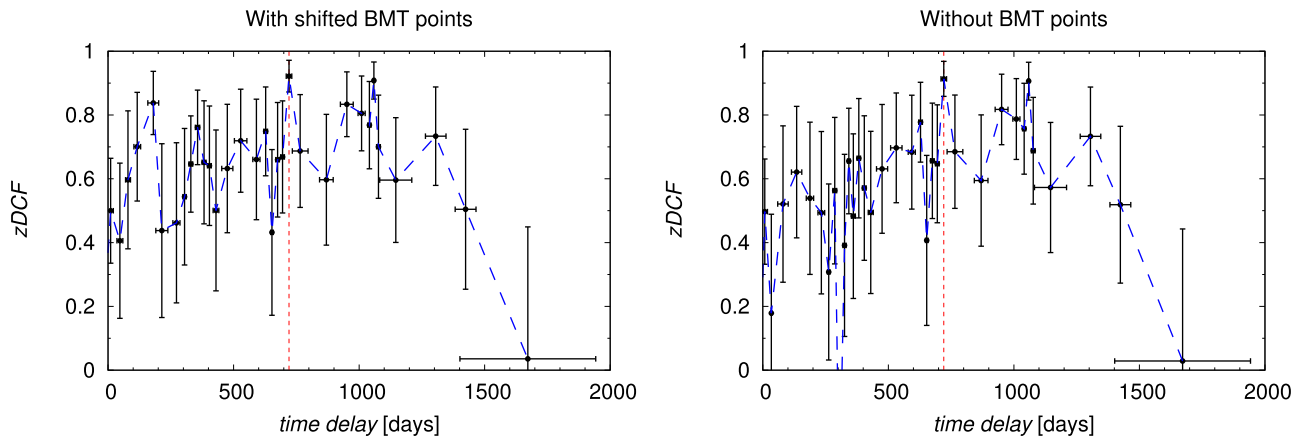

Figure B4. The zDCF values as a function of the time-delay, including the uncertainties for the time-delay and the zDCF values. Left panel: zDCF values as a function of the time-delay in the observer's frame based on the continuum lightcurve (including OGLE, SALTICAM, and flux-corrected BMT data) and Mg II line-emission lightcurve (SALT telescope). The red dashed vertical line denotes the most prominent peak at 721 days. Right panel: zDCF values vs. the time-delay in the observer's frame as in the left panel, but without BMT data points.

Table B3
Maximum-likelihood (ML) Analysis for the zDCF Time-delay Values with and Without Flux-shifted BMT Points Included

Time-delay Interval	With Shifted BMT Data	Without BMT Data
500–1000 days	$720.9^{+78.8}_{-24.1}$, $\mathcal{L} = 0.51$	$720.9^{+80.6}_{-84.5}$, $\mathcal{L} = 0.48$
1000–1500 days	$1059.0^{+219.5}_{-22.09}$, $\mathcal{L} = 0.53$	$1059.0^{+224.9}_{-19.6}$, $\mathcal{L} = 0.54$
0–2000 days	$720.9^{+323.9}_{-527.3}$, $\mathcal{L} = 0.1434$	$720.9^{+331.3}_{-100.1}$, $\mathcal{L} = 0.12$

Note. The time-delays are expressed in light days in the observer's frame. The table contains results for the localized ML analysis, taking into account the surroundings of the two most prominent peaks at 721 and 1059 days. The lower part contains the peak of the global ML analysis in the searched interval between 0 and 2000 days. The actual maximum likelihood is denoted as $\mathcal{L}$ and its value is listed for the time-delay in each interval.

damped random walk process (DRW; Kelly et al. 2009; Kozłowski et al. 2010; MacLeod et al. 2010; Kozłowski 2016). The emission-line lightcurve is then modeled as a time-delayed, scaled, and smoothed response to the continuum stochastic variability. Based on this model assumption, JAVELIN (Just Another Vehicle for Estimating Lags In Nuclei) code was developed (Zu et al. 2011, 2013, 2016).[16] The JAVELIN package employs Markov Chain Monte Carlo (MCMC) to obtain posterior probabilities of the continuum variability timescale and amplitude. With these two parameters, distributions of three parameters—time-delay, smoothing width of the top-hat function, and scaling factor (ratio of the continuum and line-emission amplitudes $A_{\text{line}}/A_{\text{cont}}$)—that describe the line-emission lightcurve are searched for.

In Figure B5, we show the distributions of the time-delay and scaling factor in the top panels with and without (magnitude-shifted) BMT data in the left and the right panels, respectively. Both the peak and the mean of the distributions are consistent within the uncertainties, with the peak close to 1050 days.

To estimate the uncertainties for these time-delays, we ran 200 bootstrap realizations, generating randomly subsets of both

_____

[16] Please visit https://bitbucket.org/nye17/javelin/src/develop/ for more information on the code usage and application.
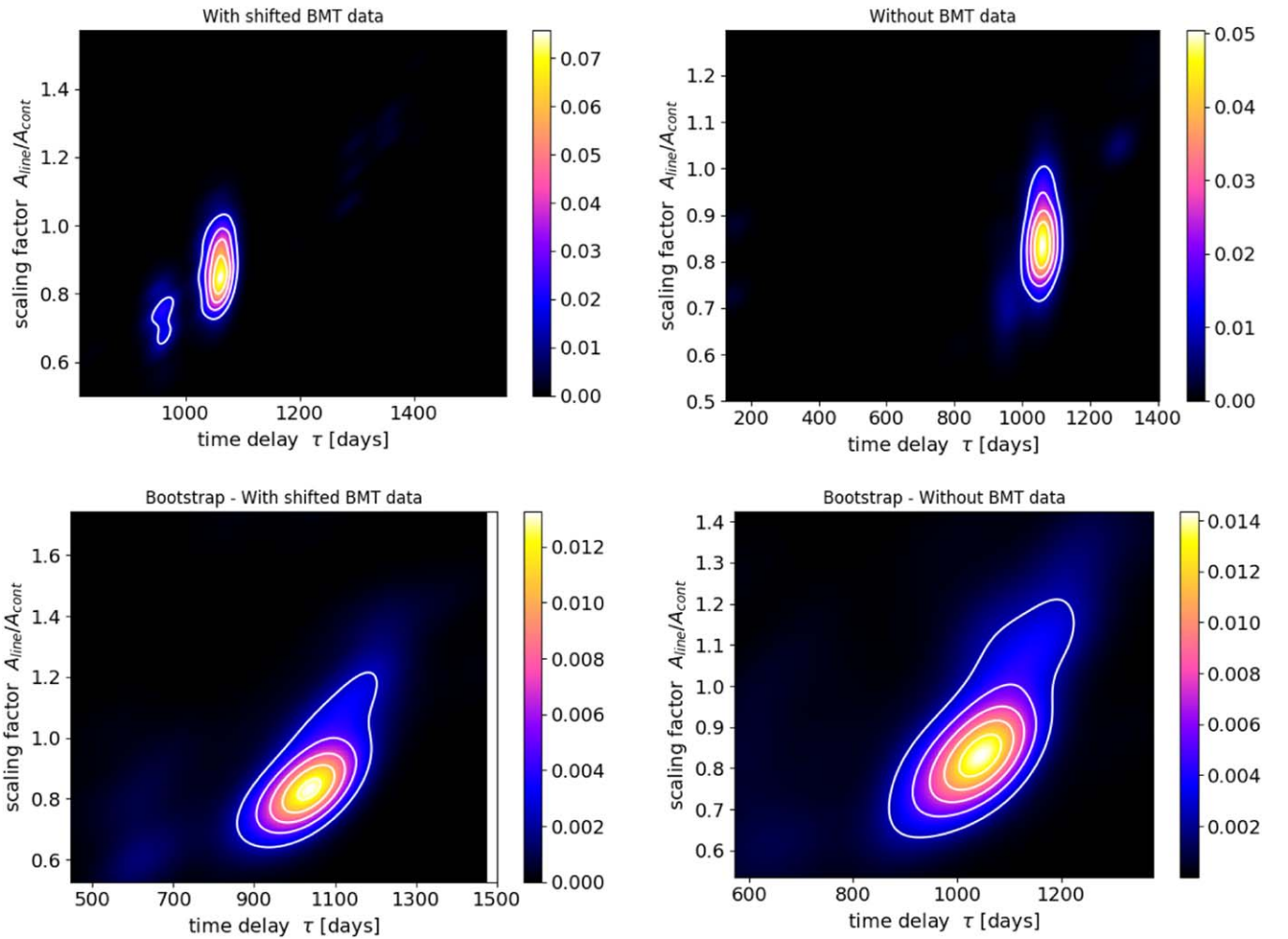
Figure B5. Color-coded plots of JAVELIN code results in the time-delay/scaling factor plane. Top row: time-delay distribution including magnitude-shifted BMT data (left panel) and without them (right panel). Bottom row: distribution of the time-delay mean values from 200 bootstrap realizations—including shifted BMT data (left panel) and without them (right panel).

lightcurves. The distributions of the means of time-delays are shown in the bottom panels of Figure B5 both with shifted BMT data (left panel) and without them (right panel). The peak and mean time-delays with corresponding uncertainties are listed in Table B4.

B.5. Measures of Regularity/Randomness—Von Neumann Estimator

A novel technique to investigate time-delays is to measure regularity or randomness of data (Chelouche et al. 2017), which has previously been extensively applied in cryptography or electronic data compression. This method does not require interpolation of lightcurves as the ICCF, nor does it require binning in the correlation space as for DCF and zDCF. Moreover, the analysis is not based on any assumptions concerning the AGN variability in a way as the JAVELIN assumes for the continuum lightcurve. One of the most robust measures of the data regularity is an optimized Von Neumann scheme, which uses the combined lightcurve $F(t, \tau) = \{(t_i, f_i)\}_{i=1}^N = F_1 \cup F_2^\tau$, where F_1 is the continuum lightcurve and F_2^τ is the time-delayed line-emission lightcurve. Based on the combined lightcurve, the Von Neumann estimator is defined as the mean successive

difference of $F(t, \tau)$,

$$E(\tau) \equiv \frac{1}{N-1} \sum_{i=1}^{N-1} [F(t_i) - F(t_{i+1})]^2. \tag{B5}$$

The minimum of the estimator E is reached for a certain time-delay $\tau = \tau'$, which is expected to be close to the actual time-delay, $\tau' = \tau_0$.

We applied the estimator to the data of HE 0413-4031 to estimate the time-delay between the continuum and Mg II line lightcurves. We made use of the Python implementation of the estimator in Equation (B5), which was demonstrated in Chelouche et al. (2017).[17] In Figure B6, we show the estimator value as a function of the time-delay with and without magnitude-shifted BMT data in the left and the right panels, respectively. For the case with shifted BMT data, we obtain the minimum of $E(\tau)$ at 499.3 days, while without BMT data, the minimum is for the time-delay of 715.18 days.

To construct distributions of the estimator minima, we perform 10,000 boostrap realizations for both cases with and without shifted BMT data. For both of these cases, the peak and the mean of the distributions are listed in Table B5. The

---

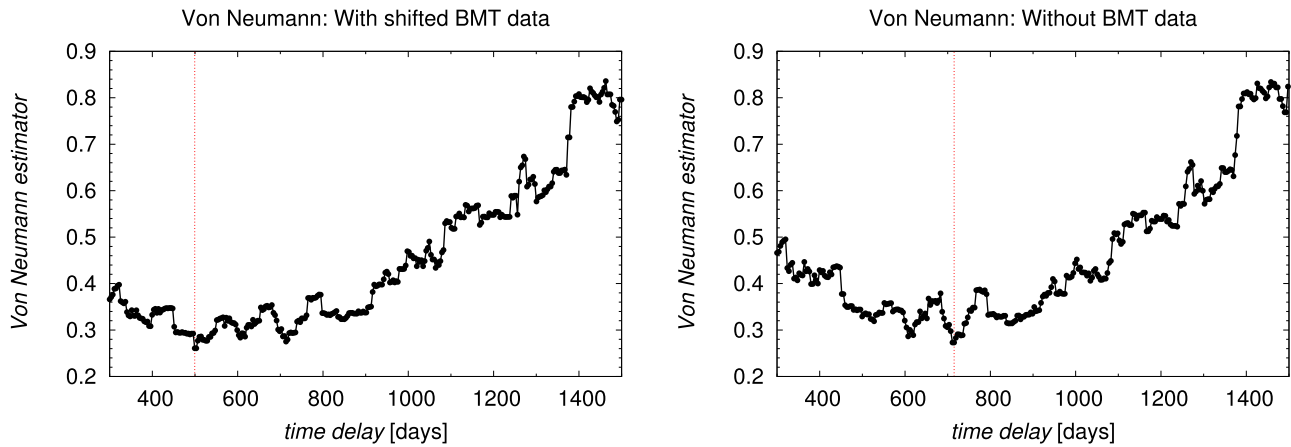[17] For the script, visit www.pozonunez.de/astro_codes/python/vnrm.py.

Figure B6. The Von Neumann estimator as a function of the time-delay. Left figure: the case with magnitude-shifted BMT data; the minimum at 499.33 days is depicted by a red vertical line. Right panel: the case without BMT data; the minimum at 715.18 days is represented by a red vertical line.
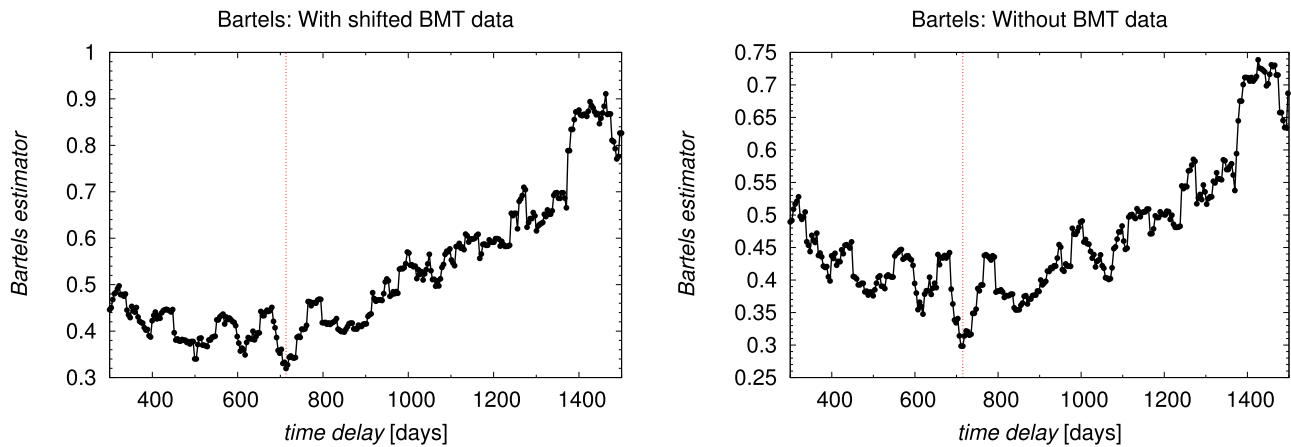

Figure B7. Bartels estimator as a function of the time-delay. Left figure: the case with magnitude-shifted BMT data; the minimum at 713.43 days is depicted by a red vertical line. Right panel: the case without BMT data; the minimum at 715.18 days is represented by a red vertical line.

Table B4
The Peak and Mean Values of the Time-delay Distribution (in the Observer's Frame) from 200 Bootstrap Realizations of JAVELIN

	With Shifted BMT Data	Without BMT Data
Peak time-delay [days]	$1053.7^{+79.8}_{-163.6}$	$1058.5^{+77.1}_{-150.7}$
Mean time-delay [days]	$1002.1^{+77.0}_{-161.8}$	$1016.0^{+70.5}_{-148.2}$

Note. Time-delays are expressed in light days.

minima and the peaks differ by about 200 days for the cases with and without BMT data. However, the minimum around 710 days is present for both cases, being a local minimum for the case with BMT data. This makes the peak at 710 days more robust, while we do not obtain any significant result for the peak at 1060–1070 days, which we obtained using JAVELIN and ICCF methods.

In addition, we perform the same analysis using the Bartels estimator, which is a modification of the Von Neumann estimator using the ranked unified lightcurve $F_R(t, \tau)$ (Bartels 1982). In comparison with the pure Von Neumann scheme, the Bartels modification of the estimator has a consistent global minimum at 713.43 and 715.18 days for both cases with and without BMT photometry data, respectively; see

Figure B7 (left and right panels, respectively). The peak values of the time-delay distribution in the observer's frame are also comparable; see Table B5. The mean value of the time-delay distribution is smaller for the case with the BMT data included, but within uncertainties the mean values of the time-delay are still comparable.

B.6. χ^2 Method

As for the quasar CTS C30.10 (Czerny et al. 2019), we also apply the χ^2 method to the lightcurves. It was found that the χ^2 method, which is frequently used in quasar lensing studies, works better than the ICCF for the AGN variability modeled as a red noise process (Czerny et al. 2013). The lightcurves were prepared as for the standard ICCF, that is, mean values were subtracted from them and they were normalized by their corresponding variances. Subsequently, the spectroscopic lightcurve was time-shifted with respect to the photometry lightcurve. The data points were linearly interpolated, but because the photometry lightcurve is denser than the spectroscopic lightcurve, we interpolated the photometry to the spectroscopy, i.e., we performed an asymmetric interpolation. Finally, we estimated the degree of similarity between shifted lightcurves by calculating the χ^2, whose minimum may be considered as the most likely time-delay between the continuum and the line emission.
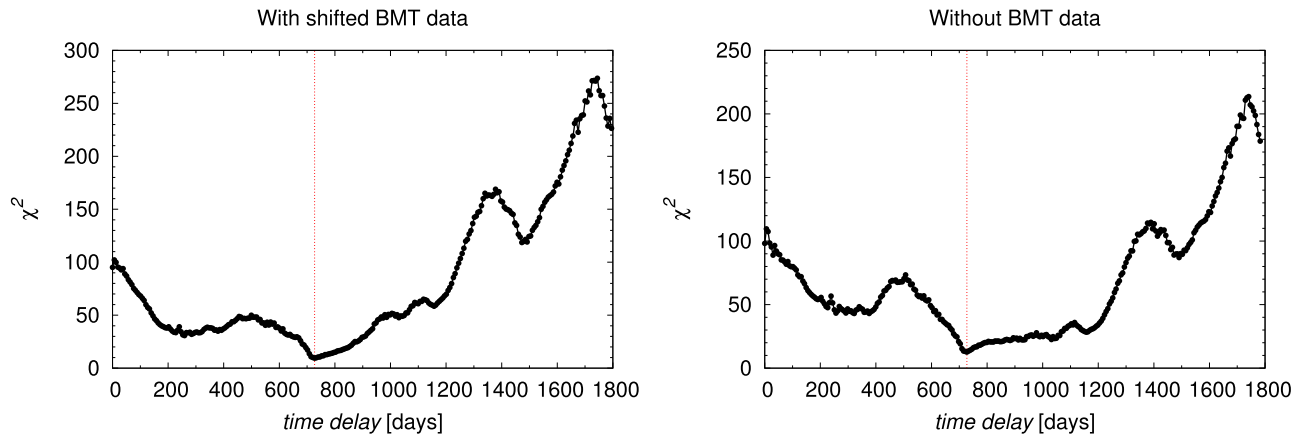
Figure B8. The values of the χ^2 statistic as a function of the time-delay expressed in days with respect to the observer's frame of reference. Left panel: the χ^2 values calculated for the case with the shifted BMT photometry data. Right panel: the χ^2 values calculated for the case without the BMT photometry data.
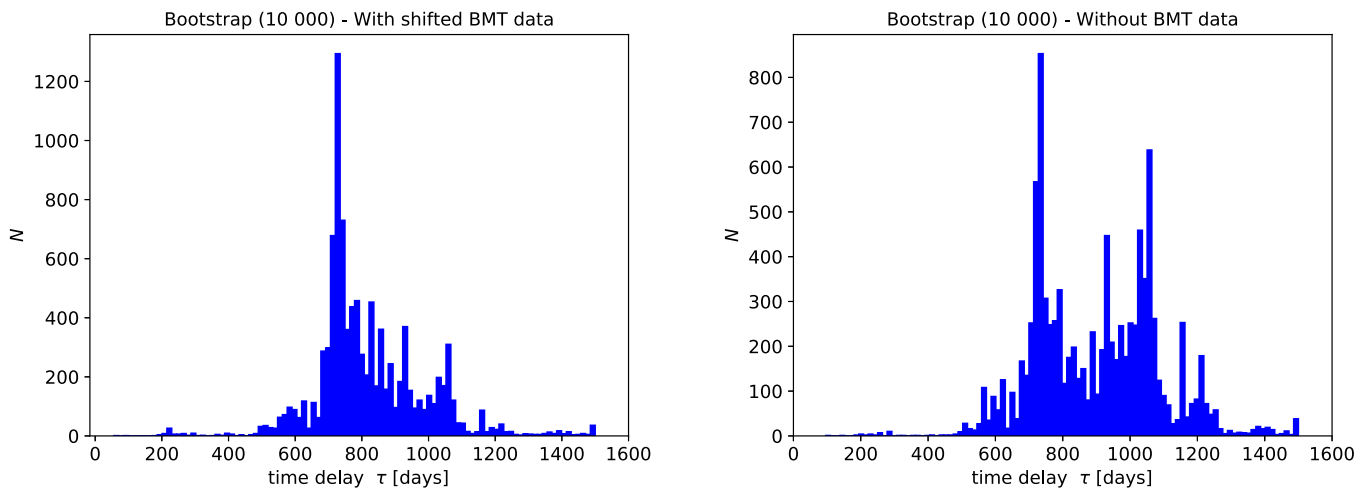

Figure B9. Distributions of the time-delays expressed in days in the observer's frame of reference for 10,000 bootstrap realizations. Left panel: the time-delay distribution based on the χ^2 analysis calculated for the case with the shifted BMT photometry data. Right panel: the time-delay distribution based on the χ^2 analysis calculated for the case without the BMT photometry data.

Table B5
The Upper Part of the Table Shows the Minima of the Von Neumann Estimator, the Peak and the Mean of Minimum Distributions for the Case With and Without Magnitude-shifted BMT Data in the Left and the Right Columns Respectively

Estimator	With Shifted BMT Data	Without BMT Data
Von Neumann: Minimum of $E(\tau)$ [days]	499.33	715.18
Von Neumann: Bootstrap (10,000)–peak [days]	$498.9^{+170.9}_{-125.9}$	$711.3^{+149.0}_{-139.5}$
Von Neumann: Bootstrap (10,000)–mean [days]	$588.5^{+157.3}_{-108.0}$	$708.1^{+147.0}_{-137.9}$
Bartels: Minimum of $E(\tau)$ [days]	713.43	715.18
Bartels: Bootstrap (10,000)–peak [days]	$710.9^{+172.3}_{-173.0}$	$714.6^{+176.1}_{-164.6}$
Bartels: Bootstrap (10,000)–mean [days]	$634.6^{+161.9}_{-159.9}$	$725.5^{+172.8}_{-150.3}$

Note. The lower part displays the same information as above, but for the Bartels estimator, which is the modification of the Von Neumann scheme using the ranked combined lightcurve. Time-delays are expressed in light days in the observer's frame.

In Figure B8, we show the χ^2 values as a function of the time-delay in the observer's frame of reference for the case with the magnitude-shifted BMT data included (left panel) and without them (right panel). In both cases, the global minimum of χ^2 is close to $\tau = 727$ days. To determine the uncertainty of this minimum, we construct the distributions of the time-delay by performing 10,000 bootstrap realizations, i.e., by creating randomly selected subsets of both lightcurves and using the χ^2 method for each new pair. The distributions are displayed in Figure B9. Both cases with and without the BMT data have one main peak and secondary peaks toward longer time-delays. The peak and mean values of the distributions are listed in Table B6. The peak and mean values are within uncertainties consistent, with the mean values shifted toward larger values with respect to the peak values because of the presence of secondary peaks at larger time-delays.

Statistic	With Shifted BMT Data	Without BMT Data
χ^2 minimum [days]	726.86	727.41
Bootstrap (10,000)– peak [days]	$720.4^{+145.6}_{-102.2}$	$727.7^{+160.0}_{-85.2}$
Bootstrap (10,000)– mean [days]	$818.6^{+133.0}_{-85.2}$	$900.0^{+110.8}_{-91.3}$

Note. We list the χ^2 minima, the peaks, and the means of the time-delay distributions expressed for the observer's frame of reference. Time-delays are expressed in light days.

Appendix C
Tests of Complementary UV Fe II Templates

We used the theoretical Fe II templates from Bruhweiler & Verner (2008) (hereafter d12 template) in our basic modeling, because one of these templates, d12-m20-20-5.dat, allowed us to get very nice and simple fits to all data sets. However, other Fe II templates are also used. Therefore, for our mean spectrum, we additionally tested two other templates. The first one was a semiempirical template of Tsuzuki et al. (2006) (hereafter T06) based on a combination of 14 low-redshift quasars and CLOUDY modeling of the Fe II emission to disentangle the Fe II and Mg II contribution. This template combined the advantage of the previously used purely observational template of Vestergaard & Wilkes (2001) and a theoretical modeling. The results are given in Table C1. The fits obtained with this template had the same number of free parameters as the fits with d12-m20-20-5.dat, if a single Lorentzian is used for Mg II, but the fit quality is always lower. The fits do not depend strongly on the doublet ratio, because the Mg II line is unresolved, and the change of the doublet ratio is easily compensated with the change of the redshift and the shift of the Mg II line with respect to the Fe II emission. Even if we add the second kinematic component, fits do not improve considerably, and final χ^2 is higher than for our canonical fits.

Next we incorporate the semiempirical UV Fe II template[18] (hereafter referred to as the KDP15 template, Kovačević-Dojčinović & Popović 2015; Popović et al. 2019) to fit the Fe II pseudo-continuum i spectral window 2700–2900 Å. This model includes overall 7 free parameters, which includes 5 multiplets, namely, 60 (a^4D–z^6F^o), 61 (a^4D–z^6P^o), 62 (a^4D–z^4F^o), 63 (a^4D–z^4D^o), and 78 (a^4P–z^4P^o). Additionally, there is an empirically added component, "I Zw 1 lines," that is represented with two Gaussians (at $\lambda\lambda$2720,2840 Å). This additional empirical set of lines was included in the model because they were not identified in the emission within $\sim$2825–2860 Å and 2690–2725 Å. The remaining parameter is the line width (see Appendix A1 in Popović et al. 2019, for more details).

The fits with this template, also given in Table C1. In the case of a single kinematic component, the provided fits are again not better in comparison with our standard fits. However, if we allow for two kinematic components for Mg II, indeed the resulting χ^2 is lower, particularly if we optimize the redshift to the new template. Although during the fitting we allowed for all the six template components to vary, we noticed in the final fits

that the multiplets 61, 63, and 78 converge to values close to zero, and only the multiplets 60 and 62 and the "I Zw 1 lines" return nonzero values. This is consistent with the Figure A1 in the paper of Popović et al. (2019). In their figure, the multiplets 60 and 78 are outside our spectral window, and the multiplet 63 has a very weak contribution (by a factor $\sim$3–3.5 times with respect to multiplet 62).

This new best fit implies a different shape of the Mg II line and different kinematics of the Fe II– and Mg II–emitting region. With d12-m20-20-5.dat, the Mg II line was represented by a single Lorentzian, and FWHM of the Mg II line was somewhat broader than the requested FWHM of the Fe II (4380 km s^{-1}, and 2800 km s^{-1}, respectively), implying that Fe II emission comes on average from a little more distant part of the BLR. In the case of the new best fit, the requested FWHM of Fe II is larger, 4000 km s^{-1}, and the two components of Mg II, if treated as separate components, have the corresponding values of FWHM of 3100 km s^{-1} and 9050 km s^{-1}, respectively, thus considerable part of the Mg II emission should originate at a larger distance than Fe II. If the two Mg II components are treated as a single asymmetric line, then the FWHM of Mg II is 4250 km s^{-1} just above that for Fe II emission in this model, but effectively similar to the FWHM of Mg II from the basic model. However, the overall line shape is widely different, and we present the new fit in Figure C1. The very broad Mg II component is then located at the same position as the Fe II emission, but the narrower Mg II component is again shifted considerably by 1545 km s^{-1} with respect to Fe II, which is comparable to the shift of 1620 km s^{-1} in our basic fits using a single Lorentzian component discussed in Section 3.1.

In addition, we verify statistically whether the fit using the KDP15 template provides an overall improvement. We compare the KDP15 template with the original fit using the d12 Fe II template, which has $p_1 = 8$ parameters (2 for Fe II, 3 for the Mg II single Lorentzian component, 2 for the power-law continuum, and 1 for the redshift). The KDP15 template uses 7 parameters for the Fe II pseudo-continuum, 5 parameters for the Mg II line with 2 Gaussian components, 2 for the power-law continuum, and 1 for the redshift, overall $p_2 = 15$ parameters. Given the $\chi_1^2 = 2088.42$ for the d12 fitting, $\chi_2^2 = 1711.34$ for the KDP15 template, and the total number of data points of $n = 579$, we can calculate the F statistic with the null hypothesis that the apparently better fit using the KDP15 template does not lead to an improvement. The F statistic can be calculated as follows

$$F = \frac{(\chi_1^2 - \chi_2^2)/(p_2 - p_1)}{\chi_2^2/(n - p_2)}, \qquad (C1)$$

which for the values above gives $F = 17.75$. When the three parameters in the KDP15 template that converge to zero are removed from the calculation, we get $F' = 31.23$. Because these values are larger than the test statistic critical value, which is between 1 and 2 for our F distribution with (7564) degrees of freedom,[19] the null hypothesis is rejected and formally, the fit using the KDP15 template with 2 Gaussian components for the Mg II line is better.

The new fit still implies a considerable shift between Fe II and Mg II components, which is not expected according to

---

[18] http://servo.aob.rs/FeII_AGN/link7.html

[19] https://www.itl.nist.gov/div898/handbook/eda/section3/eda3673.htm
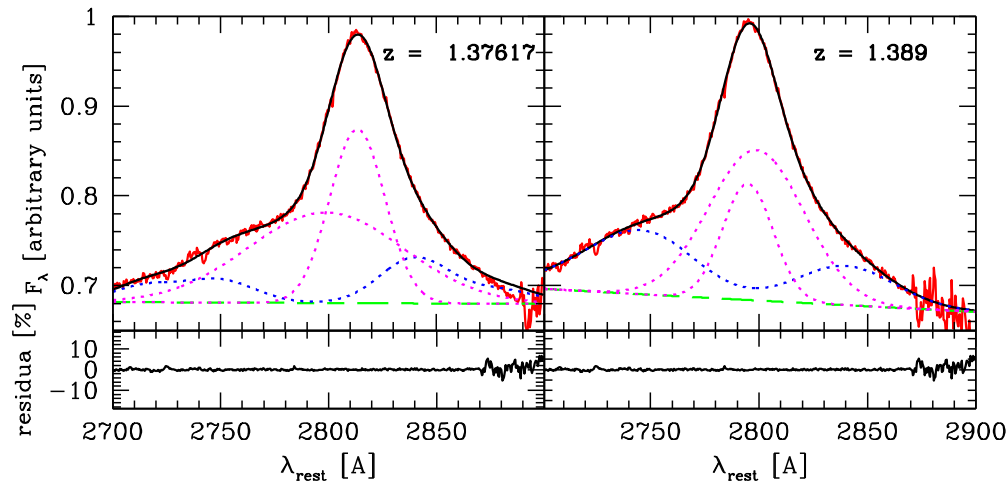
Figure C1. Left panel: the best fit to the mean spectrum with the Fe II template (Kovačević-Dojčinović & Popović, 2015; Popović et al. 2019) and 2 Gaussian components, for the best-fit redshift of 1.37617. Visually, the residuals are similar, but the implied shape of the Mg II line (dashed magenta) is very different from our standard fit shown in Figure 1. Right panel: fit of the same model but for the redshift from NED, $z = 1.389$.

Table C1
An Overview of the Parameters Used for Fitting Different Fe II Templates to the Mean Spectrum as Well as the Inferred Best-fit Parameters

Fe II Template	Mg II Shape Shape	Redshift	Doublet Ratio	Fe II Smear Velocity [km s^{-1}]	EW(Mg II)	χ^2
d12	1 Lorentz	1.37648	1.6	2800	27.44	2088.42
T06	1 Lorentz	1.38205	1.0	4500	29.64	2476.92
T06	1 Lorentz	1.38323	1.7	4700	29.77	2482.84
T06	2 Lorentz	1.38323	1.7	4700	29.74	2299.37
KDP15	1 Lorentz	1.37648*	1.6	5000	25.45	2921.12
KDP15	2 Gauss	1.37648*	1.6	4000	22.13	1749.18
KDP15	2 Gauss	1.37617	1.6	4000	22.46	1711.34
KDP15	2 Gauss	1.389 (NED)	1.6	5600	19.02	1991.62

Note. From left to right, the parameters are the template name (d12 according to Bruhweiler & Verner 2008, T06 according to Tsuzuki et al. 2006, and the KDP15 template based on Kovačević-Dojčinović & Popović, 2015; Popović et al. 2019), the Mg II shape (number of either Lorentzian or Gaussian profiles), the redshift (the star * for the KDP15 template means that the redshift was fixed in this case based on the best-fit d12 value), the Mg II doublet ratio (between one and two), Fe II smear velocity, the equivalent width of the Mg II line, and χ^2 in the last column.

Kovačević-Dojčinović & Popović (2015) and Marziani et al. (2013). However, with the KDP15 Fe II template, the fitting results highly depend on the adopted redshift. When we performed the analysis assuming that the redshift value given by NED is the right one, the decomposition of the spectrum changed significantly. Now the two Gaussians are rather similar; the dominating Gaussian coincides with the position of Fe II emission, and the second one is shifted only by 404 km s^{-1} toward shorter wavelengths. This happened because now the Fe II contribution peaks at shorter wavelengths than before, and the ratio of the multiplet 63 to multiplet 62 is 0.49, while in the previous fits the contribution from the multiplet 63 was negligible. On the other hand, formally this fit is worse, with χ^2 of 1991.62 versus 1711.34 for the redshift 1.37617. This stresses the importance of an independent and precise measurement of the redshift in this source.

Because the χ^2 for the new fit of the mean spectrum is better than our basic fit, we also refitted all individual 25 spectra using this model. Because three of the six parameters were unimportant for the mean spectrum fit, we optimize our model fitting and reduce the parameter space to account only for the contribution from these three nonzero Fe II components. The result is shown in Figure C2. The overall trend of the higher values followed with the decrease in the second part of the data
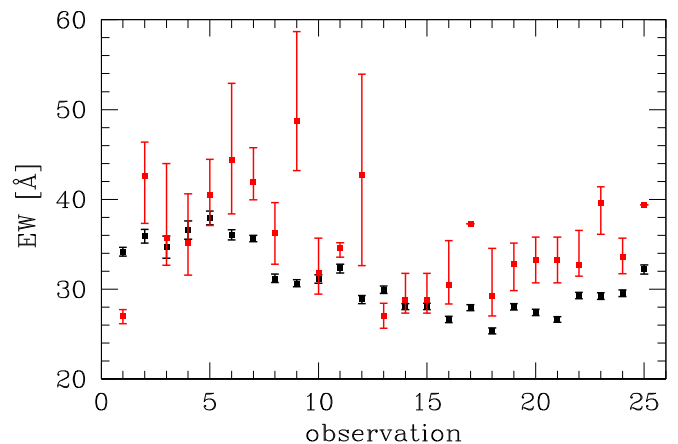

Figure C2. The equivalent width of the Mg II line in each of 25 observations measured from the standard d12 model (black points, Bruhweiler & Verner 2008) and from the new model based on the Fe II template (Kovačević-Dojčinović & Popović, 2015; Popović et al. 2019) and 2 Gaussian components. The equivalent width based on the KDP15 template has noticeably larger errors.

is still seen, but the errors are much larger. This is directly related to the larger number of parameters, and the Mg II error is determined allowing for all the other parameters to vary
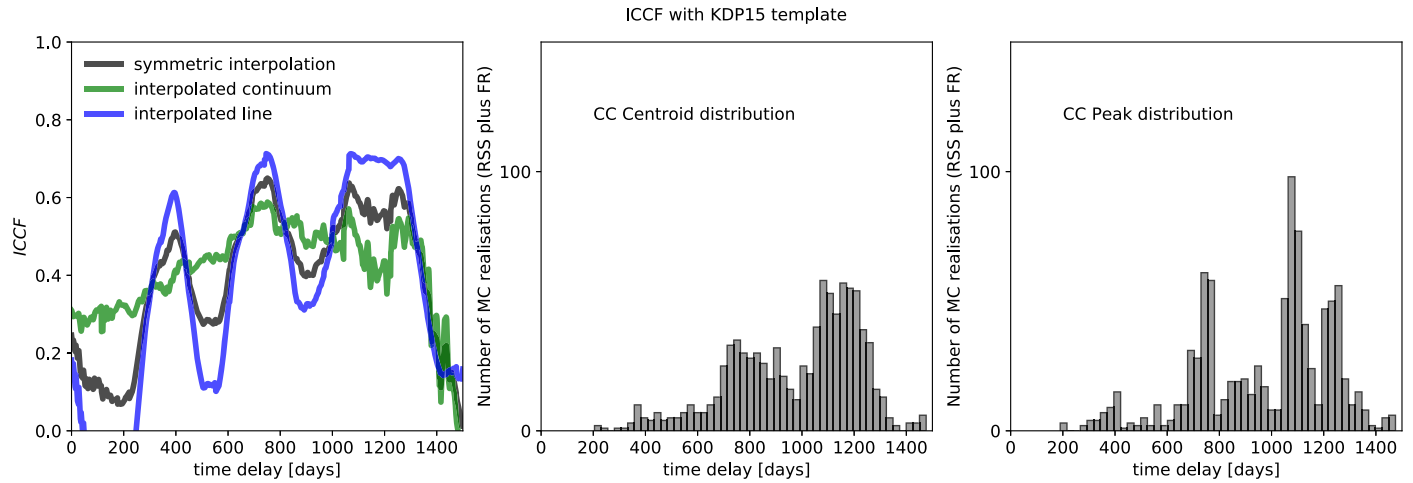
Figure C3. The ICCF values based on the KDP15 template for different interpolation cases according to the legend as a function of the time-delay in light days in the observer's frame. In the central and the right panels, we show the centroid and the peak distributions, respectively.

Table C2
The Centroid and the Peak Time-delays in Light Days in the Observer's Frame for the Mg II Lightcurve Derived from the KDP15 Template

	Centroid (days)	Peak (days)
Interpolated continuum	$1062.9^{+228.0}_{-362.3}$	$1057.5^{+247.9}_{-354.5}$
Interpolated line emission	$1070.2^{+136.9}_{-352.9}$	$1060.0^{+147.0}_{-345.6}$
Symmetric interpolation	$1058.9^{+149.0}_{-326.5}$	$1063.5^{+166.5}_{-334.5}$

Note. The values are expressed in the observer's frame for the case of the interpolated continuum lightcurve (with respect to the line emission), the interpolated line emission, and the symmetric interpolation.

(apart from the redshift, the doublet ratio, and the Fe II width, kept at values optimized for the mean spectrum). In particular, the parameters of the second, very broad component of the Mg II line are considerably degenerate with respect to the underlying power law and Fe II parameters.

The new Mg II lightcurve was used again to measure the time-delay using different methods. The values are comparable, but as expected the uncertainties are generally larger and the correlation coefficient between the two lightcurves is lower. For the ICCF, we include the centroid and the peak values for the interpolated continuum, the interpolated line emission, and the symmetric case in Table C2. In Figure C3, we show the correlation coefficient as a function of the time-delay in observer's frame with the centroid as well as the peak distributions in the central and the right panels, respectively. The peak value of the correlation coefficient is 0.65 for the time-delay of 751 days, whereas for the d12 template, we previously got the peak value of 0.86 for the time-delay of 1058 days for the case without BMT points. For the zDCF method, we obtain the peak at $\tau_{0-1000} = 382.3^{+401.1}_{-59.1}$ days according to the ML analysis in the interval of 0–1000 days. When the interval is narrowed down to 500–1000 days, the ML peak is at $\tau_{500-1000} = 765.3^{+70.2}_{-79.8}$ days, which is comparable within uncertainties to $\tau_{500-1000} = 720.9^{+80.6}_{-84.5}$ days using the d12 template without the BMT data in the same interval. The χ^2-based method gives $\tau_{d12} = 721^{+57}_{-45}$ days for the original d12 template, while for the Mg II lightcurve inferred from the KDP15 template fitting, we obtained $\tau_{KDP15} = 751^{+104}_{-150}$ days. In summary, the basic result of our

analysis—the time-delay of the response of the Mg II line—is comparable to the previous analysis based on d12 template, only the uncertainty is larger for the KDP15 template.

ORCID iDs

Michal Zajaček ⬤ https://orcid.org/0000-0001-6450-1187
Božena Czerny ⬤ https://orcid.org/0000-0001-5848-4333
Mary Loli Martinez–Aldama ⬤ https://orcid.org/0000-0002-7843-7689
Mateusz Rałowski ⬤ https://orcid.org/0000-0002-0297-3346
Aleksandra Olejak ⬤ https://orcid.org/0000-0002-6105-6492
Swayamtrupta Panda ⬤ https://orcid.org/0000-0002-5854-7426
Krzysztof Hryniewicz ⬤ https://orcid.org/0000-0002-2005-9136
Marzena Śniegowska ⬤ https://orcid.org/0000-0003-2656-6726
Mohammad-Hassan Naddaf ⬤ https://orcid.org/0000-0002-7604-9594
Grzegorz Pietrzyński ⬤ https://orcid.org/0000-0002-9443-4138
C. Sobrino Figaredo ⬤ https://orcid.org/0000-0001-9704-690X
Martin Haas ⬤ https://orcid.org/0000-0002-7284-0477
Andrzej Udalski ⬤ https://orcid.org/0000-0001-5207-5619
Marek Gorski ⬤ https://orcid.org/0000-0002-3125-9088
Marek Sarna ⬤ https://orcid.org/0000-0003-4745-3923

References

Alexander, T. 1997, in Astronomical Time Series, Vol. 218, ed. D. Maoz, A. Sternberg, & E. M. Leibowitz (Dordrecht: Kluwer), 163
Bachev, R., Marziani, P., Sulentic, J. W., et al. 2004, ApJ, 617, 171
Bahk, H., Woo, J.-H., & Park, D. 2019, ApJ, 875, 50
Baldwin, J. A. 1977, ApJ, 214, 679
Baldwin, J. A., Burke, W. L., Gaskell, C. M., & Wampler, E. J. 1978, Natur, 273, 431
Bartels, R. 1982, Journal of the American Statistical Association, 77, 40
Bennett, C. L., Larson, D., Weiland, J. L., & Hinshaw, G. 2014, ApJ, 794, 135
Bentz, M. C., Denney, K. D., Grier, C. J., et al. 2013, ApJ, 767, 149
Blandford, R. D., & McKee, C. F. 1982, ApJ, 255, 419
Bruhweiler, F., & Verner, E. 2008, ApJ, 675, 83
Burgh, E. B., Nordsieck, K. H., Kobulnicky, H. A., et al. 2003, Proc. SPIE, 4841, 1463
Carswell, R. F., & Smith, M. G. 1978, MNRAS, 185, 381

Chavushyan, V., Patiño-Álvarez, V. M., Amaya-Almazán, R. A., & Carrasco, L. 2020, ApJ, 891, 68
Chelouche, D., Pozo-Nuñez, F., & Zucker, S. 2017, ApJ, 844, 146
Code, A. D., & Welch, G. A. 1982, ApJ, 256, 1
Collin, S., Kawaguchi, T., Peterson, B. M., & Vestergaard, M. 2006, A&A, 456, 75
Collin-Souffrin, S., Dyson, J. E., McDowell, J. C., & Perry, J. J. 1988, MNRAS, 232, 539
Czerny, B. 2019, OAst, 28, 200
Czerny, B., & Hryniewicz, K. 2011, A&A, 525, L8
Czerny, B., Hryniewicz, K., Maity, I., et al. 2013, A&A, 556, A97
Czerny, B., Hryniewicz, K., Nikołajuk, M., & Sadowski, A. 2011, MNRAS, 415, 2942
Czerny, B., Olejak, A., Rałowski, M., et al. 2019, ApJ, 880, 46
Czerny, B., Siemiginowska, A., Janiuk, A., Nikiel-Wroczyński, B., & Stawarz, Ł. 2009, ApJ, 698, 840
Du, P., Lu, K.-X., Zhang, Z.-X., et al. 2016, ApJ, 825, 126
Du, P., Zhang, Z.-X., Wang, K., et al. 2018, ApJ, 856, 6
Edelson, R. A., & Krolik, J. H. 1988, ApJ, 333, 646
Elitzur, M., & Shlosman, I. 2006, ApJL, 648, L101
Forster, K., Green, P. J., Aldcroft, T. L., et al. 2001, ApJS, 134, 35
Fraix-Burnet, D., Marziani, P., D'Onofrio, M., & Dultzin, D. 2017, FrASS, 4, 1
Ganci, V., Marziani, P., D'Onofrio, M., et al. 2019, A&A, 630, A110
Gaskell, C. M. 2009, NewAR, 53, 140
Goad, M. R., Koratkar, A. P., Axon, D. J., Korista, K. T., & O'Brien, P. T. 1999, ApJL, 512, L95
Goad, M. R., Korista, K. T., & Ruff, A. J. 2012, MNRAS, 426, 3086
Grier, C. J., Trump, J. R., Shen, Y., et al. 2017, ApJ, 851, 21
Guo, H., Shen, Y., He, Z., et al. 2020, ApJ, 888, 58
Ho, L. C., Goldoni, P., Dong, X.-B., Greene, J. E., & Ponti, G. 2012, ApJ, 754, 11
Kaspi, S., Smith, P. S., Netzer, H., et al. 2000, ApJ, 533, 631
Kelly, B. C., Bechtold, J., & Siemiginowska, A. 2009, ApJ, 698, 895
Kobulnicky, H. A., Nordsieck, K. H., Burgh, E. B., et al. 2003, Proc. SPIE, 4841, 1634
Kokubo, M. 2015, MNRAS, 449, 94
Kollatschny, W., & Zetzl, M. 2011, Natur, 470, 366
Kollatschny, W., & Zetzl, M. 2013a, A&A, 549, A100
Kollatschny, W., & Zetzl, M. 2013b, A&A, 558, A26
Korista, K. T., & Goad, M. R. 2000, ApJ, 536, 284
Korista, K. T., & Goad, M. R. 2004, ApJ, 606, 749
Kovačević-Dojčinović, J., & Popović, L. Č. 2015, ApJS, 221, 35
Popović, L. Č., Kovačević-Dojčinović, J., & Marčeta-Mandić, S. 2019, MNRAS, 484, 3180
Kozłowski, S. 2015, AcA, 65, 251
Kozłowski, S. 2016, ApJ, 826, 118
Kozłowski, S., Kochanek, C. S., Udalski, A., et al. 2010, ApJ, 708, 927
Lančová, D., Abarca, D., Kluźniak, W., et al. 2019, ApJL, 884, L37
León-Tavares, J., Chavushyan, V., Patiño-Álvarez, V., et al. 2013, ApJL, 763, L36
Lira, P., Kaspi, S., Netzer, H., et al. 2018, ApJ, 865, 56
MacLeod, C. L., Ivezić, Ž, Kochanek, C. S., et al. 2010, ApJ, 721, 1014
Mao, P., Urry, C. M., Massaro, F., et al. 2016, ApJS, 224, 26
Marconi, A., Axon, D. J., Maiolino, R., et al. 2009, ApJL, 698, L103
Martínez-Aldama, M. L., Czerny, B., Kawka, D., et al. 2019, ApJ, 883, 170
Marziani, P., Dultzin, D., Sulentic, J. W., et al. 2018, FrASS, 5, 6
Marziani, P., Sulentic, J. W., Plauchu-Frayn, I., & del Olmo, A. 2013, A&A, 555, A89
McLure, R. J., & Dunlop, J. S. 2004, MNRAS, 352, 1390
McLure, R. J., & Jarvis, M. J. 2002, MNRAS, 337, 109
Mejía-Restrepo, J. E., Lira, P., Netzer, H., Trakhtenbrot, B., & Capellupo, D. M. 2018, NatAs, 2, 63
Metzroth, K. G., Onken, C. A., & Peterson, B. M. 2006, ApJ, 647, 901

Nenkova, M., Sirocky, M. M., Ivezić, Ž, & Elitzur, M. 2008, ApJ, 685, 147
Netzer, H. 2019, MNRAS, 488, 5185
Novikov, I. D., & Thorne, K. S. 1973, in Black Holes (Les Astres Occlus), ed. C. DeWitt & B. S. DeWitt (New York: Gordon and Breach), 343
Osterbrock, D. E., & Pogge, R. W. 1985, ApJ, 297, 166
Padovani, P., Alexander, D. M., Assef, R. J., et al. 2017, A&ARv, 25, 2
Panda, S., Czerny, B., Adhikari, T. P., et al. 2018, ApJ, 866, 115
Panda, S., Czerny, B., Done, C., & Kubota, A. 2019a, ApJ, 875, 133
Panda, S., Martínez-Aldama, M. L., & Zajaček, M. 2019b, FrASS, 6, 75
Pâris, I., Petitjean, P., Ross, N. P., et al. 2017, A&A, 597, A79
Patiño Álvarez, V., Torrealba, J., Chavushyan, V., et al. 2016, FrASS, 3, 19
Peterson, B. M., Ferrarese, L., Gilbert, K. M., et al. 2004, ApJ, 613, 682
Peterson, B. M., & Horne, K. 2004, AN, 325, 248
Peterson, B. M., Wanders, I., Horne, K., et al. 1998, PASP, 110, 660
Pogge, R. W., & Peterson, B. M. 1992, AJ, 103, 1084
Rakić, N., la Mura, G., Ilić, D., et al. 2017, A&A, 603, A49
Richards, G. T., Lacy, M., Storrie-Lombardi, L. J., et al. 2006, ApJS, 166, 470
Robertson, D. R. S., Gallo, L. C., Zoghbi, A., & Fabian, A. C. 2015, MNRAS, 453, 3455
Shen, Y., Hall, P. B., Horne, K., et al. 2019, ApJS, 241, 34
Shen, Y., Horne, K., Grier, C. J., et al. 2016, ApJ, 818, 30
Shen, Y., & Liu, X. 2012, ApJ, 753, 125
Shen, Y., Richards, G. T., Strauss, M. A., et al. 2011, ApJS, 194, 45
Smith, M. P., Nordsieck, K. H., Burgh, E. B., et al. 2006, Proc. SPIE, 6269, 62692A
Średzińska, J., Czerny, B., Hryniewicz, K., et al. 2017, A&A, 601, A32
Sulentic, J. W., Marziani, P., & Dultzin-Hacyan, D. 2000, ARA&A, 38, 521
Sun, M., Grier, C. J., & Peterson, B. M. 2018, PyCCF: Python Cross Correlation Function for reverberation mapping studies, Astrophysics Source Code Library, ascl:1805.032
Tadhunter, C. 2016, A&ARv, 24, 10
Tody, D. 1986, Proc. SPIE, 627, 733
Tody, D. 1993, in ASP Conf. Ser. 52, IRAF in the Nineties, ed. R. J. Hanisch, R. J. V. Brissenden, & J. Barnes (San Francisco, CA: ASP), 173
Trakhtenbrot, B., & Netzer, H. 2012, MNRAS, 427, 3081
Tsuzuki, Y., Kawara, K., Yoshii, Y., et al. 2006, ApJ, 650, 57
Ulrich, M.-H., Maraschi, L., & Urry, C. M. 1997, ARA&A, 35, 445
Vanden Berk, D. E., Richards, G. T., Bauer, A., et al. 2001, AJ, 122, 549
Véron-Cetty, M. P., & Véron, P. 2001, A&A, 374, 92
Vestergaard, M., & Osmer, P. S. 2009, ApJ, 699, 800
Vestergaard, M., & Peterson, B. M. 2006, ApJ, 641, 689
Vestergaard, M., & Wilkes, B. J. 2001, ApJS, 134, 1
Wampler, E. J., Gaskell, C. M., Burke, W. L., & Baldwin, J. A. 1984, ApJ, 276, 403
Wang, J.-M., Du, P., Li, Y.-R., et al. 2014a, ApJL, 792, L13
Wang, J.-M., Qiu, J., Du, P., & Ho, L. C. 2014b, ApJ, 797, 65
Wilhite, B. C., Vanden Berk, D. E., Kron, R. G., et al. 2005, ApJ, 633, 638
Wisotzki, L., Christlieb, N., Bade, N., et al. 2000, A&A, 358, 77
Woo, J.-H. 2008, AJ, 135, 1849
Yang, Q., Shen, Y., Chen, Y.-C., et al. 2020, MNRAS, 493, 5773
Zajaček, M., Busch, G., Valencia-S., M., et al. 2019a, A&A, 630, A83
Zajaček, M., Czerny, B., Martínez-Aldama, M. L., & Karas, V. 2019b, AN, 340, 577
Zajaček, M., Eckart, A., Britzen, S., & Czerny, B. 2019c, arXiv:1911.12901
Zheng, W., Kriss, G. A., Telfer, R. C., Grimes, J. P., & Davidsen, A. F. 1997, ApJ, 475, 469
Zhu, D., Sun, M., & Wang, T. 2017, ApJ, 843, 30
Zu, Y., Kochanek, C. S., Kozłowski, S., & Peterson, B. M. 2016, ApJ, 819, 122
Zu, Y., Kochanek, C. S., Kozłowski, S., & Udalski, A. 2013, ApJ, 765, 106
Zu, Y., Kochanek, C. S., & Peterson, B. M. 2011, ApJ, 735, 80